Bosonic field digitization for quantum computers

Alexandru Macridin, Andy C. Y. Li, Stephen Mrenna, and Panagiotis Spentzouris
Fermilab, P.O. Box 500, Batavia, Illinois 60510, USA

(Received 24 August 2021; revised 15 February 2022; accepted 19 April 2022; published 4 May 2022)

Quantum simulation of quantum field theory is a flagship application of quantum computers that promises to deliver capabilities beyond classical computing. The realization of quantum advantage will require methods that can accurately predict error scaling as a function of the resolution and parameters of the model and that can be implemented efficiently on quantum hardware. In this paper, we address the representation of lattice bosonic fields in a discretized field amplitude basis, develop methods to predict error scaling, and present efficient qubit implementation strategies. A low-energy subspace of the bosonic Hilbert space, defined by a boson occupation number cutoff, can be represented with exponentially good accuracy by a low-energy subspace of a finite-size Hilbert space. The finite representation construction and the associated errors are directly related to the accuracy of the Nyquist-Shannon sampling and the finite Fourier transforms of the boson number states in the field and the conjugate-field bases. We analyze the relation between the boson mass, the discretization parameters used for wave function sampling, and the finite representation size. Numerical simulations of small size Φ^4 problems demonstrate that the boson mass optimizing the sampling of the ground state wave function is a good approximation to the optimal boson mass yielding the minimum low-energy subspace size. However, we find that accurate sampling of general wave functions does not necessarily result in accurate representation. We develop methods for validating and adjusting the discretization parameters to achieve more accurate simulations.

DOI: 10.1103/PhysRevA.105.052405

I. INTRODUCTION

Numerical simulations of systems with continuous variables, whether classical or quantum, require digitization and truncation approximations. For a simulation to be useful, it is essential to know the limit and effect of these approximations. The impact of discretization is especially important when the computational resources required for simulation are scarce. This is a concern for present and near-future quantum computations and classical simulation of complex systems. For example, in the case of strongly correlated systems and lattice field theories, complex schemes are developed [1,2] to extrapolate the finite-size results to the thermodynamic and continuous limits. Unlike the parameters defining the physical problem under investigation, the parameters defining the algorithm (discretization parameters, cutoffs, number of iterations, etc.) should be chosen by the user to optimize the efficiency of the simulations. To do this, criteria are needed to assess whether the choice of these parameters is valid and procedures are needed to adjust them for higher accuracy when necessary. In this paper, we present digitization procedures for bosonic fields, investigate the errors introduced by these procedures and the errors' dependence on the discretization's parameters, and introduce a guide for validating and adjusting the discretization's parameters using feedback from quantum simulations.

Quantum computing offers a change of paradigm for numerical simulations. Many-body and field theory simulations, severely limited on classical computers by the exponentially large memory requirement or the insurmountable Monte Carlo sign problem, might be feasible on future quantum computers. Nevertheless, due to the characteristics of the hardware used for quantum computations, quantum algorithms require a radically different way of storing, manipulating and measuring the information compared to classical computations. As a consequence, specific methods are needed for error analysis, benchmarking, and validation.

In a commonly used approach for the numerical simulation of continuous field theories, especially for High Energy Physics problems, the space (or the time-space) coordinates are discretized and the continuous theory is mapped to a lattice field theory. The lattice field problem is solved numerically with the best methods available. The continuous field results are obtained by extrapolating the lattice spacing to zero. This procedure is well studied in the literature and is *not* the subject of this work. In condensed matter problems, the lattice is given by the physical crystalline structure, and this procedure might not even be necessary. A different approach, which *is* the focus of this paper, involves the discretization and the truncation of the field amplitude and the representation of the lattice field with qubits.

Systems with bosonic degrees of freedom arise in the Standard Model (Higgs field, gauge fields) and in the low-energy effective models describing collective excitations in condensed matter physics (phonons, magnons, plasmons, etc.). One challenge in developing quantum algorithms for bosonic systems is related to the truncation of the Hilbert space, since, unlike fermion or spin systems, boson systems can have an unbounded occupation number. While it is easy to map a truncated Hilbert space onto the qubit space in a boson number basis, it is difficult to efficiently implement the evolution operator in this basis for many models of interest (such as

relativistic scalar field models and electron-phonon systems). For this reason, truncation and discretization in the field amplitude basis have been considered. The first quantum algorithm for scalar field theories using field amplitude discretization was proposed by Jordan *et al.* [3,4]. Their error analysis, based on the Chebyshev's inequality for estimating the probability to have large amplitude fields, implies a number of discretization points per site that scales as $O(\epsilon^{-1})$, where ϵ is the field truncation error. In fact [5–8], the number of the discretization points scales exponentially better than this, i.e., $O(\log_2(\epsilon^{-1}))$, when the wave function is restricted to a low-energy subspace defined by a boson number cutoff. This is a consequence of the properties of the Hermite-Gauss functions [6,7] when using Nyquist-Shannon sampling.

The main focus of this paper is the representation of the lattice bosonic fields on the finite space of the quantum hardware. By *representation* of a bosonic field on qubits, we mean two things: (1) a mapping of the bosonic wave functions to qubit wave functions and (2) an isomorphic mapping of the bosonic field operators to discrete field operators acting on the qubit space.

The paper starts with a general overview of the main results and concepts, in Sec. II. Section III builds upon the work presented in Refs. [6,7] and addresses the construction of the finite representation in the field amplitude basis. It extends the previous work by providing a thorough analysis of the errors associated with this construction and investigating the relation between the sampling errors of the field-variable wave function and the boson truncation. By *errors* in this paper, we mean only the theoretical errors related to the boson field representation on qubits. We do not consider other errors specific to quantum simulations that arise from Trotterization, qubit decoherence, gate fidelity, control noise, etc. The construction of the finite Hilbert space is possible because (1) the boson number wave functions both in the field and the conjugate-field bases can be accurately sampled in a finite number of points, which is a consequence of the Nyquist-Shannon sampling theorem applied to *almost* band-limited and field-limited functions [9–11] and (2) the field and the conjugate-field sampling sets can be accurately connected via a finite Fourier transform. The accuracy of the finite representation depends upon the errors arising from sampling, the finite Fourier transform and the truncation introduced by the boson number cutoff. The dimension of the finite Hilbert space is the same as the number of the sampling points. The low-energy subspace is spanned by the boson number states below a cutoff. For a fixed cutoff, the errors decrease exponentially with increasing number of the sampling points. Empirically, we find that an accuracy $\epsilon \approx 10^{-4}$ requires a finite Hilbert space dimension that is two times larger than the dimension of the low-energy subspace. Many interesting problems, including the broken symmetry phase of the Φ^4 field model and the intermediate and the strongly coupled regimes of electron-phonon systems, can be addressed with no more than six qubits per lattice site. However, a word of caution is appropriate. While accurate representation implies accurate sampling, the converse statement is not true. We present examples of functions that can be sampled with great accuracy but have a significant component outside the low-energy subspace. The action of the discrete field operators on states outside the low-energy subspace yields uncontrollable errors. Therefore, a measurement of the boson distribution is necessary to ensure that the wave function in a quantum simulation belongs to the low-energy subspace.

The second part of the paper (Sec. IV) addresses the choice of the discretization parameters in quantum simulations. Different choices of the discretization and sampling intervals correspond to different choices of the boson mass and boson vacuum. The optimal choice of the boson mass corresponds to the minimal boson number cutoff since this choice also implies the minimal size of the finite Hilbert space and implicitly the smallest number of required qubits for implementation. The optimal boson mass is interaction-dependent and it is not known *a priori*. While finding the optimal boson mass by minimizing the boson number cutoff is impractical, finding the boson mass that maximizes the accuracy of the wave function's sampling is feasible, requiring only local field measurements. By employing exact diagonalization methods for small size Φ^4 problems in different parameter regimes, we find that the boson mass providing optimal sampling corresponds to the optimal boson mass.

In the third part of this paper (Sec. V), we describe measurement methods for the local field and the conjugate-field distributions and additionally for the local boson distribution. We also introduce a practical guide for adjusting and validating the discretization parameters using the feedback from quantum simulation measurements. The guideline follows a simple procedure. First, based on the field distribution measurements, the sampling intervals are adjusted to minimize the sampling errors. The optimal sampling intervals determine the number of discretization points and the boson mass to be used in further simulations, provided that these parameters yield a measured boson distribution below the cutoff. Otherwise, the number of the discretization points is increased. Note that the boson distribution measurement is not needed during the optimization process, but only as a final check after the discretization parameters are adjusted.

In Sec. VI we discuss the applicability of the discretization method presented here to quantum problems written in the first quantization formalism and the challenges for implementing bosonic algorithms on present and future quantum computers.

Section VII contains our conclusions.

II. OVERVIEW

The objective of our work is to present a comprehensive study of bosonic field digitization on quantum computers. We present our methodology in great detail to allow the readers to build their own models and perform calculations for specific problems. However, in this section we present a general overview of the main results and concepts.

A general assumption for our method is that the problem of interest can be addressed accurately by restricting the Hilbert space to a finite low-energy subspace defined by a cutoff of maximum N_b bosons per lattice site.

While qubit encoding of the boson number states is straightforward (employing, for example, a binary representation of the boson number), the implementation in the boson number basis of the Trotter step operators corresponding to

the field-dependent interaction terms requires a lengthy decomposition in single and two qubit gates, as discussed in Sec. III A. The implementation of these Trotter steps is much simpler in the field amplitude basis, since the Hamiltonian's field-dependent terms are diagonal in this basis. However, representing the truncated low-energy subspace in the field amplitude basis has its challenges, caused mainly by the fact that the field amplitude basis is a continuous and unbounded set. Controlled discretization and truncation procedures are required. We address the construction of the bosonic field representation in the field amplitude basis in Sec. III B.

We start constructing the representation of a local Hilbert space in Sec. III B 1 and then, in Sec. III B 2, the representation for the lattice field is constructed as a direct product of local (one at each lattice site) representations. The construction of the local representation is based on the discretization properties of the Hilbert space's vectors in the field amplitude basis. In this basis the vectors are equivalent to square integrable functions. Their weight at large argument decreases fast with increasing the argument. The same statement is true for the Fourier transform of these functions. The Nyquist-Shannon sampling theorem can be employed to approximate these functions and, as well, their Fourier transforms. A field variable wave function can be reconstructed with $O(\epsilon)$ accuracy from its value in a finite set of sampled points. Analogous the Fourier transform of the wave function can be reconstructed with $O(\epsilon)$ accuracy from its values in a finite set of conjugated-field sampled points. The set of field sampling points and the set of conjugate-field sampling points are related with $O(\epsilon)$ accuracy via a finite Fourier transform. The error $O(\epsilon)$ can be decreased by increasing the width of the field and conjugate-field sampling windows. In Appendixes B 1 and C 2 we calculate upper bounds for the sampling errors, relating these bounds to the wave function's weight outside the field and conjugate-field sampling windows.

To construct the local representation we focus on the sampling properties of boson number states written in the field amplitude basis. Both the boson number states in the field amplitude basis and their Fourier transforms are proportional to Hermite-Gauss functions. For a cutoff N_b and an accuracy ϵ a finite number of discretization points $N_\varphi > N_b$ can be chosen such that all boson states with $n < N_b$ can be sampled with $O(\epsilon)$ accuracy in N_φ field-variable points or N_φ conjugate-field-variable points. The sampling and the recurrence properties of the Hermite-Gauss functions allows us to define a N_φ finite-size Hilbert space $\tilde{\mathcal{H}}$ and discrete version of the field and conjugate-field operators, $\tilde{\Phi}$ and $\tilde{\Pi}$, acting on $\tilde{\mathcal{H}}$. On the subspace of $\tilde{\mathcal{H}}$ spanned by the first N_b eigenvectors of the discrete harmonic oscillator Hamiltonian [i.e., constructed with the discrete field operators, $\tilde{\Phi}$ and $\tilde{\Pi}$; see Eq. (45)] the discrete field operators obey the canonical commutation relation $[\tilde{\Phi}, \tilde{\Pi}] = iI + O(\epsilon)$. For a problem of interest, as long as N_b is taken large enough such that the contribution of the boson states with $n > N_b$ can be neglected, the infinite Hilbert space can be replaced by $\tilde{\mathcal{H}}$ and the field operators Φ and Π can be replaced by $\tilde{\Phi}$ and $\tilde{\Pi}$ with $O(\epsilon)$ accuracy. The number of the qubits required for a local representation is $n_q = \log_2(N_\varphi)$. The representation for a N site lattice field, requires $N \log_2(N_\varphi)$ qubits.

In practice it is essential to quantify and control the errors. In the last part of Sec. III B 1 a numerical analysis of the errors involved in the construction of the finite representation is presented. For $N_\varphi = 64$, $N_\varphi = 128$, and $N_\varphi = 256$ we calculate the sampling errors and the error associated with the commutations relation of the discrete field operators. These errors are proportional to the tail weights of the boson number states outside sampling interval windows. For a fixed N_b the representation error can be reduced exponentially by increasing the number N_φ of the discretization points. The ratio N_b/N_φ belongs to $[0.3, 0.7]$ when the error is in the range $[10^{-5}, 10^{-3}]$. For example, a finite representation with an accuracy of order 10^{-4} can be obtained by taking $N_\varphi = 2N_b$. Encoding this representation requires only one extra qubit (per site) when compared to the encoding in the boson number basis.

The relation between the sampling accuracy of a general wave function and its projection onto the low-energy subspace defined by the boson number cutoff is further addressed in Sec. III C. While belonging to the low-energy subspace implies accurate sampling (consequence of the representation's construction described in Sec. III B), we find that the converse is not true. We present two examples of functions with small tail weights outside sampling intervals which can be discretized with very good accuracy but have significant weight onto the subspace spanned by boson states with $n > N_b$. As a consequence, the discrete field operators acting on these functions produce uncontrollable errors. Accurate discretization of bosonic field wave functions is not enough to ensure the accuracy of the numerical simulations. Boson number distribution measurements are required to ensure the wave function belongs to the low-energy subspace.

The construction of the field amplitude representation depends on the definition of bosons, which is not unique. The boson creation and annihilation operators depends on the mass parameter. Different mass bosons are related by a squeezing operator (Bogoliubov transformation). Different choices of the boson mass correspond to different representations. A representation which requires the smallest truncation cutoff N_b for a given accuracy is optimal, since it requires the smallest amount of resources for algorithm implementation.

In principle the optimal boson mass can be determined by optimizing the boson distribution as a function of the mass parameter. However, this approach is impractical, since boson distribution measurement is expensive in quantum simulations. On the other hand the measurements of the local field and conjugate-field distribution are straightforward (as discussed in Sec. V A). Calculating the sampling windows which minimize the sampling errors of the wave function is much easier than optimizing the boson mass for the smallest cutoff N_b. In Sec. IV we investigate the relation between the optimal sampling intervals and the optimal boson mass.

For a given number of the discretization points, the sampling and finite Fourier transform errors are the smallest when the weight of the wave function outside the field sampling interval F equals the weight of the wave function's Fourier transform outside the conjugate-field sampling interval K. For this choice of the sampling intervals, is the ratio K/F, which equals the representation's boson mass, the same as the optimal boson mass? While we don't know the answer in general,

numerical simulation for small size lattices find the answer to be *yes* in many cases. Several examples are presented.

The harmonic oscillator case is illustrated first in Sec. IV A. The optimal boson mass is equal to the harmonic oscillator mass parameter m_0, since in this case the ground state is the vacuum state. When the boson mass m_1 is larger (smaller) than m_0, for a fixed truncation error, the cutoff number N_b increases linearly with increasing the ratio m_1/m_0 (m_0/m_1). The optimal boson mass can be obtained by optimizing the sampling errors. The ratio $K/F = m_0$ when F and K are chosen such that the the weight of the wave function outside the interval F equals the weight of the wave function's Fourier transform outside the interval K.

Two examples of interacting systems, a local ϕ^4 scalar field (Sec. IV B 1) and a two-site ϕ^4 scalar field with imaginary mass (Sec. IV B 2) are also presented. In both cases the ground state local field distribution is narrower than the local conjugate-field distribution. Optimal sampling requires the ratio K/F to be larger than the Hamiltonian mass parameter. The ratio K/F determined this way agrees with the optimal boson mass obtained by optimizing the boson number distribution.

In order to enhance the fidelity of applications using our methodology, procedures for validating and adjusting the discretization parameters N_φ and m for optimal performance, using feedback from quantum simulations, are presented in Sec. V. The procedures require measurements of the local field distribution, the local conjugate-field distribution and the local boson distribution. These measurements, described in Sec. V A, are local, involving the register of $\log_2(N_\varphi)$ qubits assigned to encode the bosonic field at one lattice site. The field and conjugate-field distributions require a direct measurement of the qubits. The boson distribution measurement is more laborious. We present two methods for the boson distribution measurement. The first one employs quantum state tomography [12,13] of the local qubit register of size $\log_2(N_\varphi)$. The second method is done by employing Quantum Phase Estimation method [13,14] for a local harmonic oscillator and requires an ancillary register of $\log_2(N_\varphi)+1$ qubits. The boson distribution can be measured with great accuracy since the energy levels of a harmonic oscillator are equidistant. The probability of having bosons above the cutoff N_b is given by the probability to measure integers larger than N_b in the ancillary register.

Finally, to support efficient utilization of compute resources, a practical guide for adjusting the discretization parameters in order to improve quantum simulation's performance is proposed in Sec. V B. The initial discretization intervals are determined by assuming a mean-field value for the boson mass. Simulations are run and the local field and conjugate-field distributions are measured. The sampling intervals are adjusted to optimally cover the regions where the field and the conjugate-field distribution have significant support. New simulations which measure the boson distribution are run. If the number of bosons above the cutoff N_b is negligible (i.e., it is of the order of the desired accuracy) the discretization parameters are good and the simulation's results can be trusted. Otherwise the number of the discretization points N_φ should be increased to accommodate for a larger cutoff N_b.

III. LOW-ENERGY SUBSPACE REPRESENTATION

The Hilbert space of a lattice bosonic field is a direct product of local Hilbert spaces at each lattice site. Every local Hilbert space is infinite dimensional, but for most problems can be represented by a finite subspace that contains the relevant degrees of freedom. In general, the relevant degrees of freedom depend on the problem under investigation. In this work, we study the low-energy physics of a field theory where a cut off N_b on the boson occupation number can be imposed at each site, such that the states with more than N_b bosons per site can be safely neglected. First, we briefly discuss the problems associated with the representation of the bosonic field in the boson occupation number basis. Then we address the bosonic field representation in the field amplitude basis.

A. Representation in the occupation number basis

The lattice boson number states are a direct product of single site boson number states. At each site the boson number states $|n\rangle$ are eigenstates of the harmonic oscillator Hamiltonian:

$$H_h = \frac{1}{2}\Pi^2 + \frac{1}{2}m_0^2\Phi^2 = m_0\left(a^\dagger a + \frac{1}{2}\right). \tag{1}$$

The creation and the annihilation operators, $a^\dagger$ and a, are related to the field operators by

$$\Phi = \frac{1}{\sqrt{2m_0}}(a + a^\dagger) \quad \text{and} \quad \Pi = -i\sqrt{\frac{m_0}{2}}(a - a^\dagger) \tag{2}$$

and $|n\rangle = \frac{1}{\sqrt{n!}}a^{\dagger n}|0\rangle$, where $|0\rangle$ is the boson vacuum state.

The boson number basis has been used extensively for numerical simulations of bosonic fields on classical computers. For field theories, it is intuitive to define a low-energy subspace by introducing a cutoff N_b in the boson number states. The cutoff is chosen such that the states with more than N_b bosons have a negligible contribution to the low-energy physics. In general, the cutoff N_b depends on the interaction type and strength, but also on the boson mass parameter m_0, as can be seen in Eq. (2). A particular choice of the boson mass m_0 makes the most efficient use of the computational resources, as we will discuss in Sec. IV.

At each site, boson number states truncated to a cutoff N_b can be easily encoded on $n_q = \log_2(N_b)$ qubits of a quantum computer. For example, a binary representations of the integer number n can be used. Different encodings are also possible [15]. However, quantum computation using the boson number representation is difficult to implement in models with field-amplitude-dependent coupling when the cutoff N_b is of the order of 10 or larger (i.e., when $n_q > 3$). For example, let's consider coupling terms such as $\sum_{\langle j,l\rangle}\Phi_j\Phi_l$ present in Φ^4 theory or in the phonon models, where j and l are nearest-neighbor lattice site indices. The correspondent Trotter step unitary operator,

$$e^{-i\theta\Phi_j\Phi_l} = e^{-i\frac{\theta}{2m_0}\left(a_j^\dagger a_l^\dagger + a_j^\dagger a_l + a_j a_l^\dagger + a_j a_l\right)}, \tag{3}$$

has a dense matrix representation. Since a general unitary of size k requires $O(4^k)$ CNOT gates [16–18] this Trotter step requires a lengthy decomposition with $O(4^{2n_q})$ two-qubit gates (in this case $k = 2n_q$ because bosons at two different sites are

involved). Similarly, the Trotter step operators for $\frac{\lambda}{4!}\sum_j \Phi_j^4$ interaction in Φ^4 theory or for electron-phonon coupling in phonon models requires a decomposition with $O(4^{n_q})$ two-qubit gates (in this case bosons at only one site are involved, hence $k = n_q$).

For weakly interacting problems with small number of bosonic excitations, quantum algorithms implemented using a boson number representation for the bosonic field might be feasible. The study of different encoding schemes presented in Ref. [15] finds that the efficiency of a particular encoding is heavily dependent on the model and on the truncation cutoff. In this study we propose a finite representation suitable for quantum algorithms addressing both weakly and strongly interacting field theories.

B. Representation in the field amplitude basis

We consider first the local field construction and then we extend it to lattice field.

1. *Representation of the local Hilbert space*

In this section, we address the finite representation of local Hilbert space at a particular lattice site. The local Hilbert space is specified by the field and the conjugate-field operators, Φ and Π, satisfying the canonical commutation relation

$$[\Phi, \Pi] = iI. \tag{4}$$

The local Hilbert space admits continuous bases, such as the field and the conjugate-field variable ones, and denumerable bases. In the field variable basis, the local Hilbert space is the space of the square integrable functions, $L^2(\mathbb{R})$. The boson number states, discussed in Sec. III A, are an example of a denumerable basis.

Considering the difficulties associated with the implementation of Trotter step operators for field-amplitude-dependent interaction terms in the boson number basis, a more convenient basis for quantum computation is the field amplitude basis $\{|\varphi\rangle\}$. Here $\{|\varphi\rangle\}$ are the eigenvectors of the field operator, i.e., $\Phi|\varphi\rangle = \varphi|\varphi\rangle$. The field-dependent interaction terms and the corresponding Trotter step operators are diagonal in this basis and easy to implement in a quantum algorithm [6,7,19]. However, the eigenvectors $\{|\varphi\rangle\}$ are Schwartz distributions and not proper vectors of the Hilbert space. The eigenspectrum of the field operators is continuous and unbounded, but a representation suitable for quantum computation requires discretization and truncation procedures. An apparent difficulty to introducing a finite representation for field operators is caused by their commutation relations. It is known (see, for example, Ref. [20]) that the canonical commutation relations cannot be satisfied on a finite dimensional space, since on a finite dimensional space the trace of the left-hand side of Eq. (4) is zero and the trace of the right-hand side is not. However, we construct (see Sec. III B 1 b) a finite Hilbert space $\tilde{\mathcal{H}}$ with a dimension N_φ larger than the boson number cutoff N_b to represent the low-energy subspace of dimension N_b. We define the field operators $\tilde{\Phi}$ and $\tilde{\Pi}$ on the finite Hilbert space such that $[\tilde{\Phi}, \tilde{\Pi}]I_{N_b} = iI_{N_b}$, where I_{N_b} is the projector operator onto the low-energy subspace spanned by the first N_b eigenvectors of the harmonic oscillator Hamiltonian. The algebra generated by the operators $\tilde{\Phi}$ and $\tilde{\Pi}$ is isomorphic with the algebra generated by Φ and Π, when both are restricted to the low-energy subspace.

The construction of the finite representation in the field amplitude basis is based on the discrete sampling of the square integrable functions, which is discussed in the next section.

a. Nyquist-Shannon sampling of wave functions. The field amplitude representation of the low-energy subspace is directly related to the discretization and the truncation of wave functions belonging to $L^2(\mathbb{R})$ space. The discretization procedure takes advantage of the fact that the weight of the square integrable functions at large argument is small and decreases with increasing argument.

To simplify our analysis we consider arbitrary wave functions $f(\varphi) \in S(\mathbb{R})$, where $S(\mathbb{R})$ is the Schwartz space containing the smooth and rapidly decaying functions. The Schwartz space is dense in $L^2(\mathbb{R})$ [21–23]. The Fourier transform

$$\hat{f}(\kappa) = \frac{1}{\sqrt{2\pi}} \int_{-\infty}^{\infty} f(\varphi) e^{-i\kappa\varphi}\, d\varphi \tag{5}$$

also belongs to $S(\mathbb{R})$.

We introduce the field limiting projector on the interval $[-F, F]$

$$P_F = \int_{-F}^{F} |\varphi\rangle\langle\varphi|\, d\varphi \tag{6}$$

and the tail vector

$$\left|w_F^f\right\rangle = (1 - P_F)|f\rangle \equiv Q_F|f\rangle, \tag{7}$$

with $|f\rangle = \int f(\varphi)|\varphi\rangle\, d\varphi$. The norm of $|w_F\rangle$ is equal to the tail weight of $f(\varphi)$ outside the interval $[-F, F]$,

$$\left\|w_F^f\right\| = \left(\int_{-\infty}^{-F} |f(\varphi)|^2\, d\varphi + \int_{F}^{\infty} |f(\varphi)|^2\, d\varphi\right)^{\frac{1}{2}}. \tag{8}$$

Similarly, we introduce the conjugate-field limiting (we will also call it band-limiting borrowing a signal processing common nomenclature) projector on the interval $[-K, K]$,

$$P_K = \int_{-K}^{K} |\kappa\rangle\langle\kappa|\, d\kappa, \tag{9}$$

and the tail vector

$$\left|w_K^f\right\rangle = (1 - P_K)|f\rangle \equiv Q_K|f\rangle. \tag{10}$$

The norm of $|w_K^f\rangle$ is equal to the tail weight of $\hat{f}(\kappa)$ outside the interval $[-K, K]$,

$$\left\|w_K^f\right\| = \left(\int_{-\infty}^{-K} |\hat{f}(\kappa)|^2\, d\kappa + \int_{K}^{\infty} |\hat{f}(\kappa)|^2\, d\kappa\right)^{\frac{1}{2}}. \tag{11}$$

The tail weight of $f(\varphi)$ outside the interval $[-F, F]$ can be made as small as desired by increasing F. In the literature [9–11], functions with ϵ small tail weigh are called *almost* field-limited functions. Analogously, the tail weight of $\hat{f}(\kappa)$ outside the interval $[-K, K]$ can be made as small as desired by increasing K. The function $f(\varphi)$ is *almost* band-limited.

When $\|w_K^f\|$ is small, the vector $|f\rangle$ can be considered band-limited to a good approximation, i.e., $|f\rangle \approx P_K|f\rangle$. The Nyquist-Shannon sampling theorem [24] for band-limited

functions can be employed. The approximation for $f(\varphi)$ (see Appendix A) is

$$f(\varphi) \approx \langle\varphi|P_K|f\rangle = \sum_{i=-\infty}^{\infty} \langle\varphi_i|P_K|f\rangle u_K(\varphi-\varphi_i) \approx \sum_{i=-\infty}^{\infty} f(\varphi_i)u_K(\varphi-\varphi_i), \tag{12}$$

where

$$\varphi_i = i\Delta_\varphi, \quad \Delta_\varphi = \frac{\pi}{K}, \quad \text{and} \quad u_K(\varphi) = \operatorname{sinc}\left(\frac{\varphi}{\Delta_\varphi}\right) \equiv \frac{\sin\left(\pi\frac{\varphi}{\Delta_\varphi}\right)}{\pi\frac{\varphi}{\Delta_\varphi}}. \tag{13}$$

Moreover, $f(\varphi)$ is small for $|\varphi| > F$ when F is large. The summation in Eq. (12) can be restricted to a finite number N_φ of points

$$f(\varphi) \approx \tilde{f}_\varphi(\varphi) = \sum_{i=-\frac{N_\varphi-1}{2}}^{\frac{N_\varphi-1}{2}} f(\varphi_i)u_K(\varphi-\varphi_i), \tag{14}$$

when the condition $N_\varphi\Delta_\varphi \geqslant 2F$ is fulfilled, i.e., when the sampling points cover the window interval $[-F, F]$ where f has significant support. Note that the Nyquist-Shannon theorem commonly described in the literature considers the summation index i in Eq. (12) to take integer values, but this is easily generalized to half-integer values (see Appendix A), which are more convenient for an even number of discretization points (as required by a qubit representation).

According to Eq. (14), the wave function $f(\varphi)$ can be approximated by a finite expansion of sinc functions with the coefficients equal to the value of the function in

$$N_\varphi = \left\lceil \frac{2}{\pi}FK \right\rceil \tag{15}$$

equidistant points. In Eq. (15) the notation $\lceil x\rceil$ means the *ceiling function* applied to the real number x, and is equal to the least integer greater than or equal to x. Finding analytical bounds for the accuracy of this approximation is not straightforward, see for example Ref [11]. We claim that (see Appendix B 1) a bound for Eq. (14) is

$$\|f-\tilde{f}_\varphi\| \lesssim \left\|w_K^f\right\| + \left\|w_F^f\right\| + \frac{\pi r_K^f}{2K} + \sqrt{\frac{\pi}{2K}(|f(-F)|^2+|f(F)|^2)}, \tag{16}$$

where r_K^f is the weight of $\kappa\hat{f}(\kappa)$ outside the interval $[-K, K]$,

$$r_K^f = \left(\int_{-\infty}^{-K}\kappa^2|\hat{f}(\kappa)|^2\,d\kappa + \int_K^{\infty}\kappa^2|\hat{f}(\kappa)|^2\,d\kappa\right)^{\frac{1}{2}}. \tag{17}$$

All terms in Eq. (16) vanish rapidly in the limit of large F and K for the rapidly decaying functions belonging to the Schwartz space.

Using the same reasoning, the conjugate-field variable functions can approximated by a finite expansion of N_φ sinc functions

$$\tilde{f}_\kappa(\kappa) = \sum_{p=-\frac{N_\varphi-1}{2}}^{\frac{N_\varphi-1}{2}} \hat{f}(\kappa_p)u_F(\kappa-\kappa_p), \tag{18}$$

with

$$\kappa_p = p\Delta_\kappa, \quad \Delta_\kappa = \frac{\pi}{F}, \quad \text{and} \quad u_F(\kappa) = \operatorname{sinc}\left(\frac{\kappa}{\Delta_\kappa}\right). \tag{19}$$

The vector $|\tilde{f}_\kappa\rangle$ differs from $|f\rangle$ by

$$\|f-\tilde{f}_\kappa\| \lesssim \left\|w_K^f\right\| + \left\|w_F^f\right\| + \frac{\pi r_F^f}{2F} + \sqrt{\frac{\pi}{2F}(|\hat{f}(-K)|^2+|\hat{f}(K)|^2)}, \tag{20}$$

where r_F^f is the weight of $\varphi f(\varphi)$ outside the interval $[-F, F]$,

$$r_F^f = \left(\int_{-\infty}^{-F}\varphi^2|f(\varphi)|^2\,d\varphi + \int_F^{\infty}\varphi^2|f(\varphi)|^2\,d\varphi\right)^{\frac{1}{2}}. \tag{21}$$

The accuracy of both approximations of $|f\rangle$, $|\tilde{f}_\varphi\rangle$ and $|\tilde{f}_\kappa\rangle$, is determined by the values of $f(\varphi)$ and $\hat{f}(\kappa)$ outside the intervals $[-F, F]$ and $[-K, K]$, respectively. Note that $|\tilde{f}_\varphi\rangle$ is a band-limited function and $|\tilde{f}_\kappa\rangle$ is a field-limited function, while $|f\rangle$ isn't necessary band-limited or field-limited. An approximation of $|f\rangle$ that is both band-limited and field-limited does not exist, since no analytical function, except the zero function, can be simultaneously band-limited and field-limited [10,11,25].

The vector $|f\rangle$ can be reconstructed from a set containing the field-sampled values $\{f(\varphi_i)\}_i$ or from a set containing the conjugate-field sampled values $\{\hat{f}(\kappa_p)\}_p$. The accuracy of the reconstruction is determined by the values of $|f\rangle$ outside the field and conjugate-field sampling intervals. However, accurate sampling is only a necessary condition for the representation of the bosonic field on quantum hardware. A quantum algorithm also requires implementation of unitary operators that can describe accurately the evolution of the system. While the field and conjugate-field functions $f(\varphi)$ and $\hat{f}(\kappa)$ are related by a continuous Fourier transform, the representation for bosonic fields on qubits is based on the assumption that a finite Fourier transform (FFT) connects the sampling sets $\{f(\varphi_i)\}_i$ and $\{\hat{f}(\kappa_p)\}_p$ with high precision, as will be discussed in Sec. III B 1 b.

The difference between the FFT $\tilde{\mathcal{F}}$ of the field sampling set $\{f(\varphi_i)\}_i$ denoted by $\{(\tilde{\mathcal{F}}f)(\kappa_p)\}_p$ and the function's Fourier transform in the conjugate-field sampling points $\{\hat{f}(\kappa_p)\}_p$ is determined by the weight of the function outside the sampling windows and decreases with increasing F and K. In Appendix C 1 we find that

$$\Delta_\kappa \sum_{p=-\frac{N_\varphi-1}{2}}^{\frac{N_\varphi-1}{2}} |(\tilde{\mathcal{F}}f)(\kappa_p) - \hat{f}(\kappa_p)|^2 \lesssim 2\left(\left\|w_F^f\right\|^2 + \left\|w_K^f\right\|^2\right) + \frac{\pi}{K}\left[|f(-F)|^2+|f(F)|^2\right] + \frac{\pi}{F}\left[|\hat{f}(-K)|^2+|\hat{f}(K)|^2\right]. \tag{22}$$

Similarly, the difference between the inverse finite Fourier transform of the set $\{\hat{f}(\kappa_p)\}_p$, denoted by $\{(\tilde{\mathcal{F}}^{-1}\hat{f})(\varphi_i)\}_i$, and the function at the field sampling points, $\{f(\varphi_i)\}_i$, is given by

$$\Delta_\varphi \sum_{i=-\frac{N_\varphi-1}{2}}^{\frac{N_\varphi-1}{2}} |(\tilde{\mathcal{F}}^{-1}f)(\varphi_i) - f(\varphi_i)|^2 \lesssim 2\left(\left\|w_F^f\right\|^2 + \left\|w_K^f\right\|^2\right) + \frac{\pi}{K}\left[|f(-F)|^2 + |f(F)|^2\right] + \frac{\pi}{F}\left[|\hat{f}(-K)|^2 + |\hat{f}(K)|^2\right]. \quad (23)$$

The definition of $\tilde{\mathcal{F}}$ and $\tilde{\mathcal{F}}^{-1}$ is given by Eqs. (C3) and (C4) in Appendix C 1.

b. Finite representation construction. In this section, we define the discrete field operators and construct the finite Hilbert space of the representation based on the discretization properties of the boson number states. This section ends with a detailed analysis of the errors generated by the approximations used in this construction.

Sampling of Hermite-Gauss functions. The wave functions' sampling procedures discussed in the previous section are applied here to the boson number states in the field amplitude basis. The boson number states form a denumerable basis for the local Hilbert space and provide an intuitive way to introduce the relevant low-energy subspace for the problem under investigation.

In the field amplitude basis the boson number state $|n\rangle$ is the Hermite-Gauss (HG) function of order n,

$$\langle\varphi|n\rangle \equiv \phi_n(\varphi) = \left(\frac{m_0}{\pi}\right)^{1/4} \frac{1}{\sqrt{2^n n!}} e^{-\frac{m_0\varphi^2}{2}} H_n(\sqrt{m_0}\varphi), \quad (24)$$

where H_n is the Hermite polynomial of order n. The Fourier transform of $\phi_n(\varphi)$ to the conjugate-field variable κ is also proportional to a Hermite-Gauss function of order n [26],

$$\langle\kappa|n\rangle \equiv \hat{\phi}_n(\kappa) = \frac{(-i)^n}{\pi^{1/4} m_0^{1/4} \sqrt{2^n n!}} e^{-\frac{\kappa^2}{2m_0}} H_n\left(\frac{\kappa}{\sqrt{m_0}}\right). \quad (25)$$

The recurrence properties of the HG functions [see also Eq. (2)] imply

$$\varphi\phi_n(\varphi) = \langle\varphi|\Phi|n\rangle = \frac{1}{\sqrt{2m_0}}\left(\sqrt{n}\phi_{n-1}(\varphi) + \sqrt{n+1}\phi_{n+1}(\varphi)\right), \quad (26)$$

$$\kappa\hat{\phi}_n(\kappa) = \langle\kappa|\Pi|n\rangle = -i\sqrt{\frac{m_0}{2}}\left(\sqrt{n}\hat{\phi}_{n-1}(\kappa) - \sqrt{n+1}\hat{\phi}_{n+1}(\kappa)\right). \quad (27)$$

The HG functions have significant weight on an interval centered on zero and are exponentially small at large argument, as can be inferred from Eqs. (24) and (25). The width of the window needed to contain a significant weight increases with increasing order n. Several HG functions are shown in Fig. 1 for illustration.

For a boson state $\phi_n(\varphi)$, the sampling errors appearing in Eqs. (16), (20), (22), and (23) can be written in terms of the tail weights $\|w_F^{\phi_n}\|$ and $\|w_K^{\phi_n}\|$. This can be understood by noting that $\|w_F^{\phi_n}\|$ and $\|w_K^{\phi_n}\|$ are monotonically decreasing with increasing F and K, respectively, when F and K are large enough. Therefore the dependence $F = F(\|w_F^{\phi_n}\|)$, and $K = K(\|w_K^{\phi_n}\|)$ can be found, i.e., the sampling interval widths can be expressed as function of the tail weights. As a consequence, all of the terms $r_F^{\phi_n}$, $r_K^{\phi_n}$, $|\phi_n(F)|^2$ and $|\hat{\phi}_n(K)|^2$ can be written in terms of the tail weights.

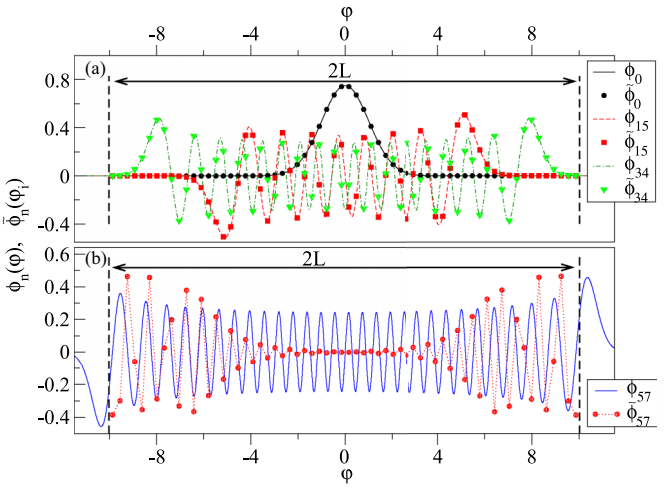

FIG. 1. (a) Hermite-Gauss functions $\phi_0(\varphi)$, $\phi_{15}(\varphi)$, and $\phi_{34}(\varphi)$ (respectively, solid, dashed, and dot-dashed lines) and the discrete harmonic oscillator (with $m_0 = 1$) eigenstates $\tilde{\phi}_0(\varphi_i)$, $\tilde{\phi}_{15}(\varphi_i)$, and $\tilde{\phi}_{34}(\varphi_i)$ (respectively, circle, square, and triangle symbols) for a finite Hilbert space with $N_\varphi = 64$ discretization points. Within $O(10^{-4})$ accuracy the support of the HG functions with $n \leqslant N_b = 34$ is inside the interval $[-L, L]$, where $L = \sqrt{\pi N_\varphi/2}$ [see Eq. (29)]. These HG functions are sampled accurately by the discrete harmonic oscillator eigenvectors. (b) The support of $\phi_{57}(\varphi)$ (solid line) has significant weight outside $[-L, L]$, and the function cannot be sampled by the eigenvector $\tilde{\phi}_{57}(\varphi_i)$ (circle symbols) of the discrete harmonic oscillator.

For HG functions, a parameter L can be defined that relates the field and conjugate-field sampling windows when $\|w_F^{\phi_n}\| = \|w_K^{\phi_n}\|$:

$$F = \frac{L}{\sqrt{m_0}}, \quad K = L\sqrt{m_0}. \quad (28)$$

The HG function $\phi_n(\varphi)$ and its Fourier transform $\hat{\phi}_n(\kappa)$ can be sampled with a finite set of points

$$N_\varphi = \left\lceil \frac{2}{\pi} FK \right\rceil = \left\lceil \frac{2}{\pi} L^2 \right\rceil, \quad (29)$$

and an error determined by the function tail weights,

$$\epsilon_w(n, L) \equiv \left\|w_F^{\phi_n}\right\| = \left\|w_K^{\phi_n}\right\|. \quad (30)$$

By considering only the leading term $2^n\varphi^n$ of the Hermite polynomial $H_n(\varphi)$, employing partial integration, and applying Stirling's formula, it can be shown that

$$\epsilon_w^2(n, L) \lesssim \frac{1}{L\sqrt{\pi}} \frac{2^n L^{2n}}{n!} e^{-L^2} \approx e^{-L^2 - \ln\sqrt{2}L\pi} e^{n\ln\frac{2eL^2}{n}} e^{-\frac{1}{2}\ln n}. \quad (31)$$

For a fixed n, the tail weight $\epsilon_w(n, L)$ decreases exponentially with increasing L. For a fixed L and $n \ll 2eL^2$, the tail weight $\epsilon_w(n, L)$ increases with increasing n. Thus, for a cutoff

N_b and an error ϵ, a parameter $L(N_b, \epsilon)$ can be chosen such that

$$\epsilon_w(n, L) < \epsilon \quad \text{for all } n < N_b. \tag{32}$$

By increasing L, the error ϵ can be decreased exponentially, i.e., $\epsilon \propto e^{-\frac{L^2}{2}+(N_b-\frac{1}{2})\ln L}$, as can be inferred from Eq. (31).

Equations (14), (16), and (32) imply that, for $n < N_b$,

$$\phi_n(\varphi) = \sum_{i=-\frac{N_\varphi-1}{2}}^{\frac{N_\varphi-1}{2}} \phi_n(\varphi_i) u_K(\varphi - \varphi_i) + O(\epsilon), \tag{33}$$

where

$$\varphi_i = i\Delta_\varphi \quad \text{and} \quad \Delta_\varphi = \sqrt{\frac{2\pi}{N_\varphi m_0}}. \tag{34}$$

Similarly, Eqs. (18), (20), and (32) imply that, for $n < N_b$,

$$\hat{\phi}_n(\kappa) = \sum_{p=-\frac{N_\varphi-1}{2}}^{\frac{N_\varphi-1}{2}} \hat{\phi}_n(\kappa_p) u_F(\kappa - \kappa_p) + O(\epsilon), \tag{35}$$

where

$$\kappa_p = p\Delta_\kappa \quad \text{and} \quad \Delta_\kappa = \sqrt{\frac{2\pi m_0}{N_\varphi}}. \tag{36}$$

The orthogonality properties of the sinc functions,

$$\int u_K(\varphi - \varphi_i) u_K(\varphi - \varphi_j)\, d\varphi = \Delta_\varphi \delta_{ij}, \tag{37}$$

and HG functions yield the following orthogonality relation

$$\Delta_\varphi \sum_{i=-\frac{N_\varphi-1}{2}}^{\frac{N_\varphi-1}{2}} \phi_n(\varphi_i)\phi_m(\varphi_i) = \delta_{nm} + O(\epsilon) \quad \text{for } n, m < N_b. \tag{38}$$

Finally, Eqs. (22), (23), and (32) imply that, for $n < N_b$, the field sampling set $\{\phi_n(\varphi_i)\}_i$ and the conjugate-field one $\{\hat{\phi}_n(\kappa_p)\}_p$ are related via a finite Fourier transform

$$\sqrt{\Delta_\kappa}\hat{\phi}_n(\kappa_p) = \frac{1}{\sqrt{N_\varphi}} \sum_{j=-\frac{N_\varphi-1}{2}}^{\frac{N_\varphi-1}{2}} \sqrt{\Delta_\varphi}\phi_n(\varphi_j) e^{-i\frac{2\pi jp}{N_\varphi}} + O(\epsilon). \tag{39}$$

Finite Hilbert space construction. The low-energy subspace of dimension N_b can be represented by a Hilbert space $\tilde{\mathcal{H}}$ of dimension $N_\varphi > N_b$, spanned by a set of orthogonal vectors $\{|\tilde{\varphi}_i\rangle\}_i$. On $\tilde{\mathcal{H}}$, we define the discrete field operator

$$\tilde{\Phi}|\tilde{\varphi}_i\rangle = \varphi_i|\tilde{\varphi}_i\rangle, \quad \text{with } \varphi_i = i\Delta_\varphi = i\sqrt{\frac{2\pi}{N_\varphi m_0}} \quad \text{and}$$
$$i = -\frac{N_\varphi - 1}{2}, -\frac{N_\varphi - 1}{2} + 1, \ldots, \frac{N_\varphi - 1}{2}, \tag{40}$$

and the discrete conjugate-field operator

$$\tilde{\Pi} = m_0 \tilde{\mathcal{F}} \tilde{\Phi} \tilde{\mathcal{F}}^{-1}, \tag{41}$$

where $\tilde{\mathcal{F}}$ is the finite Fourier transform,

$$\tilde{\mathcal{F}} = \frac{1}{\sqrt{N_\varphi}} \sum_{j,p=-\frac{N_\varphi-1}{2}}^{\frac{N_\varphi-1}{2}} e^{i\frac{2\pi}{N_\varphi}jp} |\tilde{\varphi}_j\rangle\langle\tilde{\varphi}_p|. \tag{42}$$

Note that the vectors $\{|\tilde{\kappa}_p\rangle\}_p$, obtained by applying a finite Fourier transform on $\{|\tilde{\varphi}_i\rangle\}_i$

$$|\tilde{\kappa}_p\rangle \equiv \tilde{\mathcal{F}}|\tilde{\varphi}_p\rangle = \frac{1}{\sqrt{N_\varphi}} \sum_{j=-\frac{N_\varphi-1}{2}}^{\frac{N_\varphi-1}{2}} |\tilde{\varphi}_j\rangle e^{i\frac{2\pi jp}{N_\varphi}}, \tag{43}$$

are eigenvectors of $\tilde{\Pi}$,

$$\tilde{\Pi}|\tilde{\kappa}_p\rangle = \kappa_p|\tilde{\kappa}_p\rangle \quad \text{with } \kappa_p = p\Delta_\kappa = p\sqrt{\frac{2\pi m_0}{N_\varphi}} \quad \text{and}$$
$$p = -\frac{N_\varphi - 1}{2}, -\frac{N_\varphi - 1}{2} + 1, \ldots, \frac{N_\varphi - 1}{2}. \tag{44}$$

The subspace of $\tilde{\mathcal{H}}$ spanned by the first N_b eigenvectors, $\{|\tilde{\phi}_n\rangle\}$, of the discrete harmonic oscillator Hamiltonian

$$\tilde{H}_h = \frac{1}{2}\tilde{\Pi}^2 + \frac{1}{2}m_0^2\tilde{\Phi}^2 \tag{45}$$

is a representation of the low-energy subspace of the full Hilbert space with $O(\epsilon)$ accuracy, provided that $N_\varphi\Delta_\varphi \geqslant 2F$, where F is large enough that the weight of the $n = N_b + 2$ Hermite-Gauss function outside the interval $[-F, F]$ is $O(\epsilon)$ small.

To validate our construction, consider the subspace of $\tilde{\mathcal{H}}$ spanned by the vectors $\{|\tilde{n}\rangle\}_{n<N_b+2}$ defined as

$$|\tilde{n}\rangle \equiv \sqrt{\Delta_\varphi}\sum_i \phi_n(\varphi_i)|\tilde{\varphi}_i\rangle = \sqrt{\Delta_\kappa}\sum_p \hat{\phi}_n(\kappa_p)|\tilde{\kappa}_p\rangle + O(\epsilon) \tag{46}$$

[see Eqs. (39) and (43)]. Note that the ability to relate accurately the field and conjugate-field sampling points of HG functions of order $n < N_b + 2$ by the finite Fourier transform is essential for Eq. (46). The set $\{|\tilde{n}\rangle\}_{n<N_b+2}$ is orthogonal and normalized [within $O(\epsilon)$ accuracy], as implied by Eq. (38). Moreover Eqs. (26) and (27) imply

$$\begin{aligned}\langle\tilde{\varphi}_i|\tilde{\Phi}|\tilde{n}\rangle &= \varphi_i\langle\tilde{\varphi}_i|\tilde{n}\rangle \\ &= \frac{1}{\sqrt{2m_0}}\left(\sqrt{n}\langle\tilde{\varphi}_i|\widetilde{n-1}\rangle + \sqrt{n+1}\langle\tilde{\varphi}_i|\widetilde{n+1}\rangle\right) \\ &\quad + O(\epsilon),\end{aligned} \tag{47}$$

$$\begin{aligned}\langle\tilde{\kappa}_p|\tilde{\Pi}|\tilde{n}\rangle = \kappa_p\langle\tilde{\kappa}_p|\tilde{n}\rangle &= -i\sqrt{\frac{m_0}{2}}\left(\sqrt{n}\langle\tilde{\kappa}_p|\widetilde{n-1}\rangle\right. \\ &\quad \left. - \sqrt{n+1}\langle\tilde{\kappa}_p|\widetilde{n+1}\rangle\right) \\ &\quad + O(\epsilon), \quad \text{when } n+1 < N_b+2,\end{aligned} \tag{48}$$

since, as can be deduced from Eq. (46), $\langle\tilde{\varphi}_i|\tilde{n}\rangle \propto \phi_n(\varphi_i)$ and $\langle\tilde{\kappa}_p|\tilde{n}\rangle \propto \hat{\phi}_n(\kappa_p)$. Eqs. (47) and (48) can be written as

$$\tilde{\Phi}|\tilde{n}\rangle = \frac{1}{\sqrt{2m_0}}\left(\sqrt{n}|\widetilde{n-1}\rangle + \sqrt{n+1}|\widetilde{n+1}\rangle\right) + O(\epsilon), \tag{49}$$

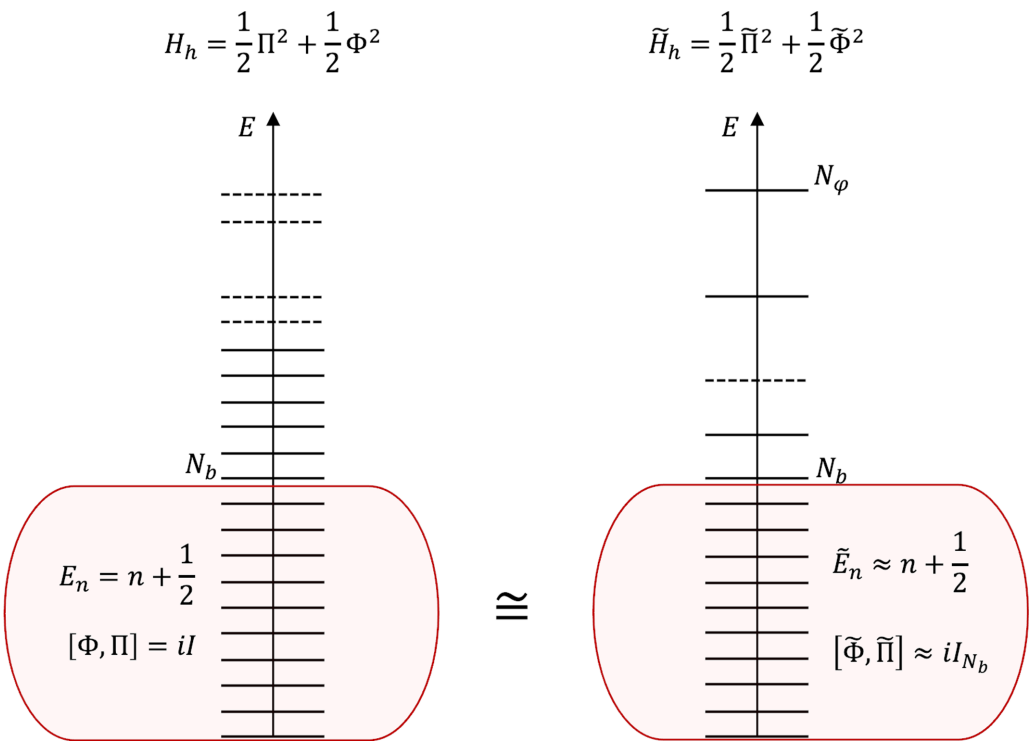

FIG. 2. Within $O(\epsilon)$ accuracy, the algebra generated by the field operator Φ and Π restricted to the N_b size low-energy subspace of the harmonic oscillator Hamiltonian (1) (shaded region, left side) is isomorphic with the algebra generated by the discrete field operators $\tilde{\Phi}$ and $\tilde{\Pi}$ restricted to the the N_b size low-energy subspace of the discrete harmonic oscillator Hamiltonian (45) (shaded region, right side). The accuracy increases exponentially with increasing the size N_φ of the finite Hilbert space; see Eq. (61).

$$\tilde{\Pi}|\tilde{n}\rangle = -i\sqrt{\frac{m_0}{2}}\left(\sqrt{n}|\widetilde{n-1}\rangle - \sqrt{n+1}|\widetilde{n+1}\rangle\right) + \times O(\epsilon), \quad \text{when } n+1 < N_b + 2. \tag{50}$$

Using Eqs. (49) and (50), it can be shown that

$$\tilde{H}_h|\tilde{n}\rangle = m_0\left(n + \frac{1}{2}\right)|\tilde{n}\rangle + O(\epsilon) \quad \text{when } n+2 < N_b + 2. \tag{51}$$

The vectors $\{|\tilde{n}\rangle\}_{n<N_b}$ are approximations of order $O(\epsilon)$ of the eigenstates of the discrete harmonic oscillator. For illustration, in Fig. 1(a) we show several eigenvectors $\{|\tilde{\phi}_n\rangle\}_{n<N_b}$ of $\tilde{H}_h$ (circle, square, and triangle symbols), obtained by exact diagonalization. As can be seen, they sample very well the HG functions plotted with lines.

Using Eqs. (49) and (50) to calculate the commutator of the discrete field operators, one gets

$$\left[\tilde{\Phi}, \tilde{\Pi}\right]|\tilde{n}\rangle = i|\tilde{n}\rangle + O(\epsilon), \quad \text{for } n < N_b. \tag{52}$$

Thus the operators $\tilde{\Phi}$ and $\tilde{\Pi}$ obey [within the error $O(\epsilon)$] the same commutation relation as Φ and Π [see Eq. (4)] on the subspace spanned by the vectors $\{|\tilde{n}\rangle\}_{n<N_b}$.

As long as the physics of the problem of interest can be addressed by truncating the number of bosons per site to N_b (i.e., N_b is taken large enough), the full Hilbert space can be replaced by the finite-size $\tilde{\mathcal{H}}$ space and the operators Φ and Π can be replaced by $\tilde{\Phi}$ and $\tilde{\Pi}$, respectively. The operators $\tilde{\Phi}$ and $\tilde{\Pi}$ act on the subspace spanned by $\{|\tilde{\phi}_n\rangle\}_{n<N_b}$ as the field operators Φ and Π act on the subspace spanned by $\{|n\rangle\}_{n<N_b}$. The situation is illustrated in Fig. 2.

Nevertheless, the high-energy eigenvectors of the finite space $\tilde{\mathcal{H}}$ have very different properties then the corresponding eigenvectors of the full Hilbert space. For example, one can see in Fig. 1(b) that the $\tilde{H}_h$ eigenvector coefficients $\langle\tilde{\varphi}_i|\tilde{\phi}_{57}\rangle$ (circle symbols) do not sample the HG function $\phi_{57}(\varphi)$ (solid line), since $\phi_{57}(\varphi)$ does not belong to the low-energy subspace when $N_\varphi = 64$. When doing numerical simulations one has to make sure that N_b and N_φ are sufficiently large that the high-energy subspace contribution to the physical problem can be safely neglected. This will be discussed more in Sec. V.

An interesting property of the discrete harmonic oscillator Hamiltonian $\tilde{\mathcal{H}}_h$, Eq. (45), is that it commutes with the FFT. By writing

$$\tilde{H}_h = \frac{1}{2}m_0^2\left(\tilde{\mathcal{F}}\tilde{\Phi}^2\tilde{\mathcal{F}}^{-1} + \frac{1}{2}\tilde{\Phi}^2\right) = \frac{1}{2}m_0^2\left(\tilde{\mathcal{F}}^{-1}\tilde{\Phi}^2\tilde{\mathcal{F}} + \frac{1}{2}\tilde{\Phi}^2\right), \tag{53}$$

it is easy to see that $[\tilde{\mathcal{H}}, \tilde{\mathcal{F}}] = 0$. The last equality in Eq. (53) is a consequence of the parity inversion symmetry of $\tilde{\mathcal{H}}$. All eigenvectors $\{|\tilde{\phi}_n\rangle\}_n$ of $\tilde{\mathcal{H}}$ (the ones belonging to the high-energy subspace too) are eigenvectors of the finite Fourier transform. This is just the discrete version of the HG functions' property of being eigenvectors of both the harmonic oscillator Hamiltonian and the continuous Fourier transform.

Error analysis. We argued previously that the errors of the finite representation are of the same order of magnitude as the weight $\epsilon_w(n, L)$ of the HG functions with $n \leqslant N_b +$

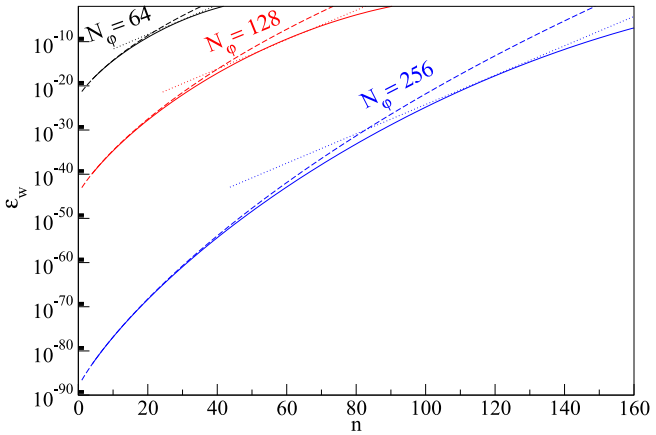

FIG. 3. Tail weight $\epsilon_w(n)$ [Eq. (30)] (solid lines) of HG functions vs n for $N_\varphi = 64$ (upper, black), $N_\varphi = 128$ (middle, red) and $N_\varphi = 256$ (lower, blue) discretization points. Equation (54) (dashed lines) is a good approximation for small $n \lesssim 0.3N_\varphi$. For larger n, $\epsilon_w(n) = \epsilon_c(n-2)/(1.5\sqrt{n(n-1)})$ with $\epsilon_c(n)$ given by Eq. (61) (dotted lines) provides a better bound for the error.

2 outside the interval $[-F, F]$. In this section we investigate numerically the errors involved in the construction of the finite representation.

Figure 3 shows the tail weight of the HG functions, $\epsilon_w[n, L(N_\varphi)]$ [see Eqs. (29) and (30)], as a function of n for $N_\varphi = 64, N_\varphi = 128$ and $N_\varphi = 256$. The tail weight is obtained by numerical integration of Eq. (8). For comparison, the tail weight approximation obtained from Eqs. (29) and (31),

$$\epsilon_w(n, N_\varphi) \approx \frac{1}{\pi\sqrt{\pi}} e^{-\frac{\pi}{4}N_\varphi} e^{\frac{2n-1}{4}\ln N_\varphi} e^{-\frac{n}{2}\ln n} e^{\frac{n}{2}(\ln\pi+1)} e^{-\frac{1}{4}\ln n}, \tag{54}$$

is shown with dashed lines. Equation (54) is a good approximation for the tail weight for $n \lesssim 0.3N_\varphi$ and overestimates $\epsilon_w(n)$ at larger values of n.

Nonzero $\epsilon_w(n)$ causes a finite difference between the discretized HG functions $|\tilde{n}\rangle$ defined by Eq. (46), and the eigenvectors of the discrete harmonic oscillator, $|\tilde{\phi}_n\rangle$. Employing exact diagonalization to calculate $|\tilde{\phi}_n\rangle$ we find that

$$\epsilon_d(n) = ||\tilde{n}\rangle - |\tilde{\phi}_n\rangle|| \tag{55}$$

is proportional to $\epsilon_w(n)$, i.e., $\epsilon_d(n) \approx 1.5\epsilon_w(n)$, as illustrated with thin continuous red and dashed red lines in Fig. 4.

Each time the field operators $\tilde{\Phi}$ and $\tilde{\Pi}$ act on the eigenvector $|\tilde{\phi}_n\rangle$ of $\tilde{H}_h$, the errors are amplified approximately by a factor of $\sqrt{n+1}$. This can be understood from Eqs. (49) and (50) when one replaces $|\widetilde{n+1}\rangle$ with $|\tilde{\phi}_{n+1}\rangle + (|\widetilde{n+1}\rangle - |\tilde{\phi}_{n+1}\rangle)$. The leading error associated with the finite magnitude of $|\widetilde{n+1}\rangle - |\tilde{\phi}_{n+1}\rangle$ is magnified by a factor $\sqrt{n+1}$. Numerical calculations agree with this assertion. For example, the state $\tilde{\Pi}|\tilde{\phi}_n\rangle$ behaves as $\Pi|n\rangle$ up to an error,

$$\epsilon_\Pi(n) = \left|\left|\tilde{\Pi}|\tilde{\phi}_n\rangle - \frac{-i}{\sqrt{2}}\left(\sqrt{n}|\tilde{\phi}_{n-1}\rangle - \sqrt{n+1}|\tilde{\phi}_{n+1}\rangle\right)\right|\right|. \tag{56}$$

As shown in Fig. 4 with dash-dot-dot green and dotted green lines, $\epsilon_\Pi(n) \approx \sqrt{n+1}\epsilon_d(n+1)$. The same conclusion

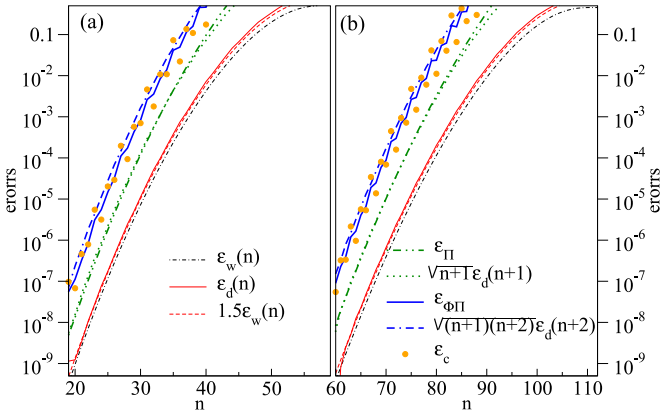

FIG. 4. The tail weight, $\epsilon_w(n)$, Eq. (30), of HG functions (dash-dot black), the difference between the discretized HG and the discrete harmonic oscillator, $\epsilon_d(n)$, Eq. (55) (thin solid red), the error associated with the $\tilde{\Pi}$ operator $\epsilon_\Pi(n)$, Eq. (56) (dash-dot-dot green), the error associated with the $\tilde{\Phi}\tilde{\Pi}$ operator $\epsilon_{\Phi\Pi}(n)$, Eq. (57) (thick solid blue), and the commutation relation error, $\epsilon_c(n)$, Eq. (58) (orange circle symbols). In good approximation $\epsilon_d(n) \approx 1.5\epsilon_w(n)$ (dashed red line), $\epsilon_\Pi(n) \approx \sqrt{n+1}\epsilon_d(n+1)$ (dotted green line), and $\epsilon_{\Phi\Pi}(n) \approx \epsilon_c \approx \sqrt{(n+1)(n+2)}\epsilon_d(n+2)$ (dot-dash-dash blue line). The size of the finite Hilbert space is (a) $N_\varphi = 64$ and (b) $N_\varphi = 128$.

is valid for the error associated with the behavior of the state $\tilde{\Phi}|\tilde{\phi}_n\rangle$ (not shown).

The error associated to the commutation relation, $[\tilde{\Phi}, \tilde{\Pi}]|\tilde{\phi}_n\rangle$, is comparable with the errors associated to the states $\tilde{\Phi}\tilde{\Pi}|\tilde{\phi}_n\rangle$ and $\tilde{\Pi}\tilde{\Phi}|\tilde{\phi}_n\rangle$. Figure 4 shows

$$\epsilon_{\Phi\Pi}(n) = \left|\left|\tilde{\Phi}\tilde{\Pi}|\tilde{\phi}_n\rangle - \frac{i}{2}\left(-\sqrt{(n-1)n}|\tilde{\phi}_{n-2}\rangle + \sqrt{(n+1)(n+2)}|\tilde{\phi}_{n+2}\rangle + |\tilde{\phi}_n\rangle\right)\right|\right|, \tag{57}$$

with a thick solid blue line, and

$$\epsilon_c = ||\left(\left[\tilde{\Phi}, \tilde{\Pi}\right] - i\right)|\tilde{\phi}_n\rangle||, \tag{58}$$

with orange dots. We find (see also the dot-dash-dash blue line) that

$$\epsilon_{\Phi\Pi}(n) \approx \epsilon_c \approx \sqrt{(n+1)(n+2)}\epsilon_d(n+2). \tag{59}$$

Since $\epsilon_w(n, N_\varphi)$ increases with increasing n, for a finite representation of size N_φ and cutoff N_b, the leading error is of the order of $\epsilon_w(N_b+2, N_\varphi)$. For a given cutoff N_b, the error can be reduced exponentially by increasing the number of discretization points N_φ, $\epsilon \propto \epsilon_w(N_b+2, N_\varphi) \leqslant e^{-\frac{\pi}{4}N_\varphi + \frac{(2N_b+3)}{4}\ln N_\varphi}$, as Eq. (54) and the numerical results shown in Fig. 3 imply.

For fixed accuracy, an increase of the low-energy subspace requires an increase of N_φ. For small N_b/N_φ the dependence between N_b and N_φ at fixed error is given by Eq. (54). The region where the accuracy is of order $\epsilon = 10^{-3}$–10^{-5} is of practical interest for simulations. In this region $N_b/N_\varphi \in \approx [0.3, 0.7]$ and Eq. (54) overestimates the errors. Numerical investigations and arguments based on the WKB approximation [6,7] indicate that, in this region

$$N_\varphi \approx c_1 + c_2 N_b, \tag{60}$$

where c_1 and c_2 are accuracy-dependent parameters. At fixed accuracy, there is a linear dependence between the size N_φ of the finite space $\tilde{\mathcal{H}}$ and the boson cutoff number N_b. For example, we find that the number of discretization points $N_\varphi \approx 32 + 1.5N_b$ for an accuracy $\epsilon = 10^{-3}$ [7]. In practice, for many problems of interest, such as scalar Φ^4 theory and electron-phonon systems, the representation in the field amplitude basis requires only one more qubit per harmonic oscillator than the representation in the boson number basis.

Numerical investigations in the region with the error range $\epsilon \in [10^{-5}, 10^{-3}]$ [7], yield the following upper bound for the error associated with the commutation relation [Eq. (58)],

$$\epsilon_c < 10e^{-(0.51N_\varphi - 0.765N_b)}. \tag{61}$$

In Fig. 3 we show with dotted lines $\epsilon_w(n) = \epsilon_c(n-2)/(1.5\sqrt{n(n-1)})$ [see the numerical dependence between ϵ_d and ϵ_c in Eq. (59)] where ϵ_c is given by Eq. (61).

2. Representation of the lattice Hilbert space

The construction of the lattice representation is a straightforward extension of the local representation construction. The lattice Hilbert space is a direct product of N local infinite Hilbert spaces,

$$\mathcal{H} = \prod_{j=1}^{N} \otimes \mathcal{H}_j \equiv L^2(\mathbb{R}^N), \tag{62}$$

where N represents the number of the lattice sites. The finite-size Hilbert space of dimension $(N_\varphi)^N$,

$$\tilde{\mathcal{H}} = \prod_{j=1}^{N} \otimes \tilde{\mathcal{H}}_j, \tag{63}$$

with $\tilde{\mathcal{H}}_j$ being the local Hilbert spaces of dimension N_φ constructed in Sec. III B 1, is a representation of the lattice low-energy subspace with maximum N_b bosons per site. The Hilbert space $\tilde{\mathcal{H}}$ is spanned by the vectors

$$\{|\tilde{\varphi}_{i_1}\rangle_1 |\tilde{\varphi}_{i_2}\rangle_2 \cdots |\tilde{\varphi}_{i_N}\rangle_N\}, \quad \text{with} \quad i_j = -\frac{N_\varphi - 1}{2}, \frac{N_\varphi - 1}{2}. \tag{64}$$

The discrete field operators are defined as

$$\tilde{\Phi}_j |\tilde{\varphi}_{i_1}\rangle_1 .. |\tilde{\varphi}_{i_j}\rangle_j \cdots |\tilde{\varphi}_{i_N}\rangle_N = i_j \Delta_\varphi |\tilde{\varphi}_{i_1}\rangle_1 \cdots |\tilde{\varphi}_{i_j}\rangle_j \cdots |\tilde{\varphi}_{i_N}\rangle_N, \tag{65}$$

$$\tilde{\Pi}_j |\tilde{\varphi}_{i_1}\rangle_1 \cdots |\tilde{\kappa}_{m_j}\rangle_j \cdots |\tilde{\varphi}_{i_N}\rangle_N = m_j \Delta_\kappa |\tilde{\varphi}_{i_1}\rangle_1 \cdots |\tilde{\kappa}_{m_j}\rangle_j \cdots |\tilde{\varphi}_{i_N}\rangle_N, \tag{66}$$

where

$$|\tilde{\varphi}_{i_1}\rangle_1 \cdots |\tilde{\kappa}_{m_j}\rangle_j \cdots |\tilde{\varphi}_{i_N}\rangle_N = \frac{1}{\sqrt{N_\varphi}} \sum_{i_j=-\frac{N_\varphi-1}{2}}^{\frac{N_\varphi-1}{2}} \sum |\tilde{\varphi}_{i_1}\rangle_1 \cdots |\tilde{\varphi}_{i_j}\rangle_j \cdots |\tilde{\varphi}_{i_N}\rangle_N e^{i\frac{2\pi i_j m_j}{N_\varphi}} \tag{67}$$

is obtained via a local Fourier transform at site j. The conjugate-field operator can be written as

$$\tilde{\Pi}_j = m_0 \tilde{\mathcal{F}}_j \tilde{\Phi}_j \tilde{\mathcal{F}}_j^{-1}, \tag{68}$$

where

$$\tilde{\mathcal{F}}_j = I_1 \otimes I_2 \otimes \cdots I_{j-1} \otimes (\tilde{\mathcal{F}})_j \otimes I_{j+1} \cdots \otimes I_N \tag{69}$$

is the finite Fourier transform acting on the local Hilbert space $\tilde{\mathcal{H}}_j$.

On the subspace spanned by

$$\{|\tilde{\phi}_{n_1}\rangle_1 |\tilde{\phi}_{n_2}\rangle_2 \cdots |\tilde{\phi}_{n_N}\rangle_N\}_{n_1,n_2,\ldots,n_N<N_b}, \tag{70}$$

where $|\tilde{\phi}_n\rangle_j \in \tilde{\mathcal{H}}_j$ is the n's' eigenvector of a discrete harmonic oscillator Hamiltonian (45), the field operators satisfy

$$\left[\tilde{\Phi}_i, \tilde{\Pi}_j\right] = \delta_{ij}[iI_i + O(\epsilon)], \tag{71}$$

where $O(\epsilon)$ represents the error of constructing local representations and was discussed in Sec. III B 1. With $O(\epsilon)$ accuracy, the algebra generated by the field operators is isomorphic with the algebra generated by the continuous field operators when restricted to the low-energy subspace defined by $n_j < N_b$ at every j site.

C. Accurately sampled states not contained in the low-energy subspace

We have described how to map a low-energy subspace of the infinite Hilbert space onto a low-energy subspace of a finite Hilbert space. The dimension N_φ of the local finite Hilbert space depends on the dimension N_b of the low-energy subspace and the accuracy ϵ.

While an accurate representation of the low-energy subspace implies accurate sampling of the low-energy wave functions, the converse is not necessarily true. Good sampling of a wave function does not imply that the wave function belongs to the low-energy subspace. There are functions that can be sampled with ϵ-accuracy in N_φ points and do not belong to the low-energy subspace of dimension $N_b(N_\varphi, \epsilon)$. Since the high-energy subspace projection of these wave functions is significant, the actions of the discrete field operators on them yield uncontrollable errors. Therefore, it is important to verify that the system wave function has a boson distribution that is below the cutoff. We describe how this can be accomplished with quantum simulations in Sec. V.

To emphasize this point, we present examples of wave functions with small tail weights outside sampling intervals that can be sampled accurately on N_φ discretization points, but have a significant high-energy weight and therefore cannot be represented accurately on a finite Hilbert space of dimension N_φ.

For the first example, we consider a band-limited function $f(\varphi)$ [see Eqs. (12) and (13)]

$$f(\varphi) = \sum_{i=-\frac{N_\varphi-1}{2}}^{\frac{N_\varphi-1}{2}} a_i u_K(\varphi - \varphi_i), \tag{72}$$

where we take $F = K = \sqrt{\pi N_\varphi/2}$ [see Eq. (15)], with $N_\varphi = 64$. As described in Appendix D, the coefficients a_i are chosen such that the behavior as $\varphi \to \infty$ is

$$f(\varphi) \sim c_f \sin\left(\frac{\pi\varphi}{\Delta_\varphi} - \frac{\pi}{2}\right)\frac{\Delta_\varphi^8}{\pi\varphi^8} + O\left(\frac{\Delta_\varphi^{10}}{\pi\varphi^{10}}\right), \tag{73}$$

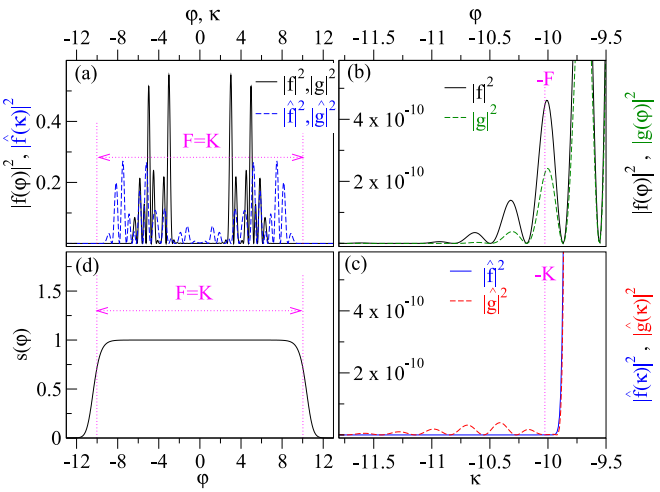

FIG. 5. (a) The square amplitude of the functions $f(\varphi)$ [Eq. (73)] and $g(\varphi)$ [Eq. (78)] (solid black) and of their Fourier transforms $\hat{f}(\kappa)$ and $\hat{g}(\kappa)$ (dashed blue), respectively. At this scale, f and g are indistinguishable. (b) $|f(\varphi)|^2$ (solid black) and $|g(\varphi)|^2$ (dashed green) for $\varphi < -F$. (c) $|\hat{f}(\kappa)|^2$ (solid blue) and $|\hat{g}(\kappa)|^2$ (dashed red) for $\kappa < -K$. The weights of both f and g outside the sampling interval is small, $\approx O(10^{-5})$. (d) The function $s(\varphi)$ [Eq. (79)] used to define $g(\varphi)$. $s(\varphi)$, and implicitly $g(\varphi)$, decay exponentially fast at large $|\varphi|$.

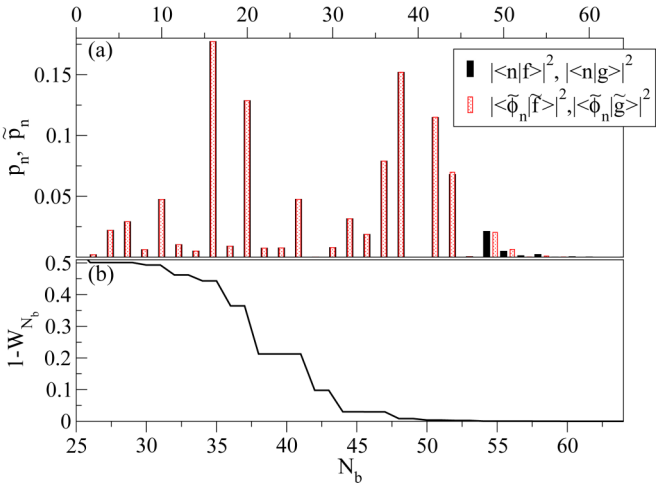

FIG. 6. (a) Boson distribution of the wave functions $f(\varphi)$ and $g(\varphi)$ (solid black). Discrete harmonic oscillator eigenstate distribution of the discretized states $|\tilde{f}\rangle$ and $|\tilde{g}\rangle$ (hashed red). At large n the boson and the discrete harmonic oscillator eigenstate distributions differ significantly. (b) The high-energy weight of the wave functions $f(\varphi)$ and $g(\varphi)$ vs the cutoff N_b. Fifty percent (20%) of the wave functions' weight belongs to the high-energy subspace spanned by states with $n > 30$ ($n > 40$).

where c_f is a normalization constant, i.e., the function decays as $|\varphi|^{-8}$ with increasing $|\varphi|$. The square amplitudes $|f(\varphi)|^2$ and $|\hat{f}(\kappa)|^2$ are plotted in Fig. 5. For $\varphi < -F$, we have $|f(\varphi)|^2 \approx O(10^{-10})$ as can be seen in Fig. 5(b). The weight outside the interval $[-F, F]$ is $\|w_F^f\| \approx 1.1 \times 10^{-5}$. Since the function is band-limited, $\hat{f}(\kappa) = 0$ for $|\kappa| > K$. By construction, the finite Fourier transform connects the sets $\{f(\varphi_i)\}_{i=\overline{-(N_\varphi-1)/2,(N_\varphi-1)/2}}$ and $\{\hat{f}(\kappa_p)\}_{p=\overline{-(N_\varphi-1)/2,(N_\varphi-1)/2}}$ without error, since, in the sampling points, the function coincides with the aliased function [see Eqs. (C1) and (C2)].

Despite the small tail weight and perfect sampling, the wave function $f(\varphi)$ cannot be represented accurately on a finite Hilbert space of size $N_\varphi = 64$. To demonstrate this, we show in Fig. 6(a) the boson distribution of the wave function $f(\varphi)$,

$$p(n) = |\langle n|f\rangle|^2 = \left| \int \phi_n(\varphi) f(\varphi)\, d\varphi \right|^2, \tag{74}$$

and in Fig. 6(b) the weight $1 - W_{N_b}$ of the high-energy subspace versus the cutoff N_b, where

$$W_{N_b} = \sum_{n<N_b} p(n). \tag{75}$$

The figure indicates a significant boson distribution for $n > N_b = 30$. In fact, we observe that 50% of the wave function belongs to the subspace spanned by boson states with $n > 30$ and 20% of the wave function belongs to the subspace spanned by boson states with $n > 40$. However, according to the data presented in Fig. 4(a), the boson number states with $n > 30$ cannot be represented with $O(10^{-5})$ accuracy on $N_\varphi = 64$ discretization points.

Due to the significant high-energy weight of $f(\varphi)$, the representation of the function on a finite space with $N_\varphi = 64$,

$$|\tilde{f}\rangle = \sum_{i=-\frac{N_\varphi-1}{2}}^{i=\frac{N_\varphi-1}{2}} f(\varphi_i)|\tilde{\varphi}_i\rangle, \tag{76}$$

yields uncontrollable errors when measurements are taken. For example, the boson distribution calculated on the finite Hilbert space using the discrete representation $\tilde{f}$ and the harmonic oscillator eigenstates $\tilde{\phi}_n$,

$$\tilde{p}(n) = |\langle \tilde{\phi}_n|\tilde{f}\rangle|^2, \tag{77}$$

is different from the real boson distribution given by Eq. (74), as illustrated in Fig. 6(a).

Since the asymptotic behavior of the wave function might impact significantly its boson distribution, we consider a second example obtained by multiplying $f(\varphi)$ with the exponentially decaying function $s(\varphi)$:

$$g(\varphi) = c_g f(\varphi) s(\varphi), \tag{78}$$

$$s(\varphi) = \frac{1}{\left(e^{-\frac{\varphi+L}{\sigma}} + 1\right)^2 \left(e^{\frac{\varphi-L}{\sigma}} + 1\right)^2}. \tag{79}$$

In Eq. (78), c_g is a normalization constant, and, in Eq. (79), we take $\sigma = 0.4$. The function $s(\varphi)$, plotted in Fig. 5(d), takes the value 1 almost everywhere inside the interval $[-F, F]$ and decays exponentially outside this interval ($s(\varphi) \propto \exp(-\varphi^2/\sigma^2)$ at large $|\varphi|$). Unlike $f(\varphi)$, which might be considered a specially chosen case, $g(\varphi)$ is a more common example. It is not band-limited or field-limited and has exponentially decaying tails. However, at the scale shown in Fig. 5(a), the functions $f(\varphi)$ and $g(\varphi)$ are indistinguishable. The difference between $f(\varphi)$ and $g(\varphi)$ can be seen in Fig. 5(b). The difference

between their Fourier transforms can be seen in Fig. 5(c). The tail weight of $g(\varphi)$ outside $[-F, F]$ is $\|w_F^g\| \approx 6 \times 10^{-6}$. Unlike $\hat{f}(\kappa)$, the conjugate variable function $\hat{g}(\kappa)$ is not zero for $\kappa > |K|$. However, its tail weight is small, $\|w_K^g\| \approx 6.2 \times 10^{-6}$. Within accuracy $O(10^{-5})$, the discrete representation of $g(\varphi)$ is the same as the one for $f(\varphi)$, $|\tilde{g}\rangle \approx |\tilde{f}\rangle$.

Despite the different asymptotic behavior of the functions $f(\varphi)$ and $g(\varphi)$ at large argument, the difference between the boson distribution of these two functions functions is very small, indistinguishable on the scale shown in Fig. 6. The differences are noticeable for $n > 80$ where the boson weight is small, of the order $O(10^{-10})$ (not shown). All the conclusions we drew about $f(\varphi)$ are valid for $g(\varphi)$ too. The wave function $g(\varphi)$ is not restricted to the low-energy subspace corresponding to $N_\varphi = 64$ and accuracy $O(10^{-5})$ and cannot be represented accurately on a finite Hilbert space of size $N_\varphi = 64$. The boson distribution $|\langle n|g\rangle|^2$ of the wave function $g(\varphi)$ differs from the boson distribution $|\langle\tilde{\phi}_n|\tilde{g}\rangle|^2$ of the discrete representation.

These two examples of functions with small tail weight at large argument, one band-limited and having algebraic decay and one with exponential decay, that can be sampled accurately but cannot be restricted to the low-energy subspace, show that the criteria of small weight at large argument is not enough for determining the size of the finite representation. It would be useful to have an estimate of the Hermite-Gauss functions expansion series for *almost* band-limited and field-limited functions as a function of the tail weights and the cutoff N_b,

$$\left\| f\rangle - \sum_{n=0}^{N_b} c_n|n\rangle \right\| \approx \mathcal{E}(N_b, \|w_F^f\|, \|w_K^f\|, \ldots). \tag{80}$$

Such an expression could be used to estimate the cutoff N_b and the number of the discretization points necessary for an accurate representation by measuring the field and conjugate-field distributions. We are not aware if an estimation like Eq. (80) exists in the literature. It is possible that combining the estimation of the prolate spheroidal wave functions expansion of *almost* band-limited functions [11] with the estimation of the Hermite-Gauss function expansion of prolate spheroidal wave functions [27] would yield an useful expression, but the problem requires further investigation.

IV. SAMPLING PARAMETERS AND THE BOSON MASS CHOICE

As discussed previously, the low-energy subspace of a bosonic field can be mapped accurately onto a low-energy subspace of a finite Hilbert space. The dimension N_φ of the local finite Hilbert space is monotonically increasing with the low-energy subspace dimension N_b. The boson number states and implicitly the cutoff N_b are dependent on the mass parameter m_0 [see Eq. (2)]. The definition of the finite Hilbert space $\tilde{\mathcal{H}}$ and of the discrete field operators depends on m_0 too, as implied by Eqs. (40) and (41). There are many possible finite representations of the bosonic field that correspond to different choices of the boson mass. The optimal representation is the one that requires the smallest cutoff N_b for the ground state and for the low-energy excitations of the system.

A. Squeezed boson states

To represent the ground state of a harmonic oscillator with mass m_0, the optimal choice for the boson mass is simply m_0, because for this choice the ground state has zero bosons (the ground state is the vacuum). However, other choices for the mass parameter can be taken, but they require more discretization points for a specified accuracy, as we discuss below. We work through this case as a prelude to more complicated Hamiltonians where the optimal choice of mass is not obvious.

The Hamiltonian (1) can be rewritten as

$$H_h = \frac{m_1}{4}\left(\frac{m_0^2}{m_1^2} - 1\right)\left(a_1^\dagger a_1^\dagger + a_1 a_1\right) + \frac{m_1}{4}\left(\frac{m_0^2}{m_1^2} + 1\right)\left(2a_1^\dagger a_1 + 1\right), \tag{81}$$

where the mass m_1 bosons are defined by

$$a_1^\dagger = \frac{1}{\sqrt{2}}\left(\sqrt{m_1}\Phi - i\frac{1}{\sqrt{m_1}}\Pi\right) \quad \text{and}$$
$$a_1 = \frac{1}{\sqrt{2}}\left(\sqrt{m_1}\Phi + i\frac{1}{\sqrt{m_1}}\Pi\right). \tag{82}$$

The relation between the mass m_1 bosons and the mass m_0 ones is given by the squeezing operation

$$a_0^\dagger = S(r)^\dagger a_1^\dagger S(r), \tag{83}$$

where

$$S(r) = e^{\frac{1}{2}r\left(a_1^{\dagger 2} - a_1^2\right)} \quad \text{and} \quad r = \frac{1}{2}\ln\left(\frac{m_1}{m_0}\right). \tag{84}$$

In the basis $\{|n\rangle_1\}_n$, where $|n\rangle_1 = \frac{1}{\sqrt{n!}}a_1^{\dagger n}|0\rangle_1$ is the state with nm_1 bosons, the harmonic oscillator ground state $|0\rangle$ is a squeezed vacuum state [28],

$$|0\rangle \equiv |0\rangle_0 = S^\dagger(r)|0\rangle_1 = \sum_{n=0}^{\infty} C_n|n\rangle_1, \tag{85}$$

$$C_{2n} = (-1)^n \frac{\sqrt{(2n)!}}{2^n n!}\frac{(\tanh r)^n}{\sqrt{\cosh r}}, \qquad C_{2n+1} = 0. \tag{86}$$

The magnitude of the coefficients C_{2n} in Eq. (86) decrease rapidly with increasing n. For any small ϵ a cutoff N_b can be introduced such that the the harmonic oscillator ground state has ϵ probability to have more than N_b m_1 bosons.

The cutoff N_b increases with increasing or decreasing $\frac{m_1}{m_0}$. In Fig. 7(a) we plot the m_1-boson distribution, $p(n; \frac{m_1}{m_0}) = p(n; \frac{m_0}{m_1}) = |C_n|^2$ as a function of n for different values of $\frac{m_1}{m_0}$. When $m_1 = m_0$ the distribution has $p(0) = 1$ and $p(n > 1) = 0$, since the ground state is the m_0 boson vacuum. The distribution weight at large n increases with increasing $\frac{m_1}{m_0}$ or $\frac{m_0}{m_1}$. The cutoff N_b is defined by requiring that $1 - W_{N_b} = \epsilon$, where W_{N_b} is the weight of the low-energy subspace spanned by the boson number states below the cutoff N_b [see Eq. (75)] and ϵ is the desired truncation error. In Fig. 7(b) we show N_b vs $\epsilon = 1 - W_{N_b}$ for different values of the squeezing parameter r. The cutoff N_b increases logarithmically with decreasing $1 - W_{N_b}$. In Fig. 7(c) we show the cutoff N_b versus r for different values of $1 - W_{N_b}$. The cutoff N_b increases exponentially

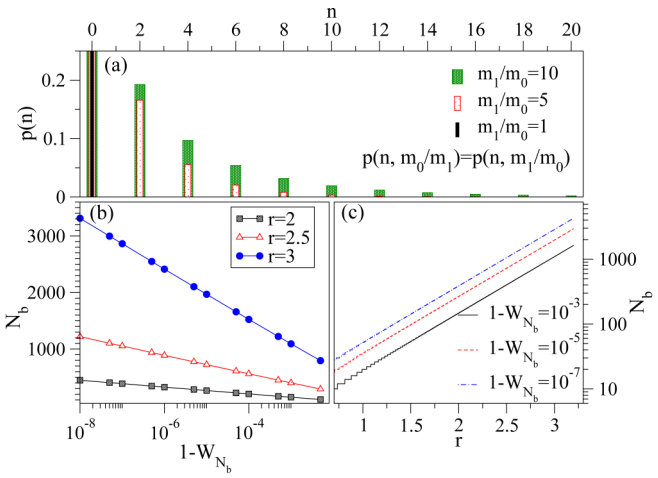

FIG. 7. (a) m_1-boson distribution of the harmonic oscillator ground state for different values of the ratio m_1/m_0. (b) Boson cutoff number N_b vs the high-energy subspace weight $1 - W_{N_b}$ for different values of the squeezing parameter $r = \frac{1}{2}\ln(\frac{m_1}{m_0})$. (c) Boson cutoff number N_b vs the squeezing parameter r for different values of $1 - W_{N_b}$. Numerical fitting yields $N_b \approx [-0.595 - 0.477 \ln(1 - W_{N_b})]\frac{m_1}{m_0}$.

with increasing r, which implies linear dependence of N_b on the boson mass m_1. Numerical fitting yields $N_b \approx [-0.595 - 0.477 \ln \epsilon]\frac{m_1}{m_0}$. Since the number of the discretization points N_φ needed to represent the low-energy subspace increases monotonically with N_b, a boson mass choice $m_1 \neq m_0$ is not optimal.

This same conclusion can be inferred just by analyzing the Nyquist-Shannon sampling parameters of the harmonic oscillator wave functions $\phi_0(\varphi)$ and $\hat{\phi}_0(\kappa)$. For a given number N_φ of discretization points, the m_0-sampling implies the sampling intervals [see Eqs. (28) and (29)]

$$F_0 = \sqrt{\frac{\pi N_\varphi}{2m_0}}, \quad K_0 = \sqrt{\frac{\pi N_\varphi m_0}{2}}, \tag{87}$$

which yield equal tail weights $\|w^{\phi_0}_{F_0}\| = \|w^{\phi_0}_{K_0}\|$. For m_1 sampling one has

$$F_1 = F_0\sqrt{\frac{m_0}{m_1}}, \quad K_1 = K_0\sqrt{\frac{m_1}{m_0}}. \tag{88}$$

For $m_1 > m_0$, the field sampling interval decreases while the conjugate-field sampling interval increases by a factor $\sqrt{m_1/m_0}$. Consequently the tail weight $\|w^{\phi_0}_{F_1}\| \gg \|w^{\phi_0}_{F_0}\|$ increases exponentially, while $\|w^{\phi_0}_{K_1}\| \ll \|w^{\phi_0}_{K_0}\|$ decreases exponentially (since the tail weights have an exponential dependence on the sampling intervals' length). Similarly, when $m_0 > m_1$ the tail weight $\|w^{\phi_0}_{F_1}\| \ll \|w^{\phi_0}_{F_0}\|$ and $\|w^{\phi_0}_{K_1}\| \gg \|w^{\phi_0}_{K_0}\|$. In both cases, because of the large increase of one of the tail weights, the finite Fourier transform that connects the field and the conjugate-field sampling sets yields a much larger error [see Eqs. (22) and (23)] than in the case of m_0 sampling. Since the error in constructing the finite Hilbert space representation is proportional to the error introduced by the finite Fourier transform [see Eq. (46)], sampling corresponding to $m_1 \neq m_0$ implies larger errors than m_0 sampling.

B. Sampling intervals

The sampling and discretization intervals depend on the boson mass and the number of the discretization points, in accordance with Eqs. (34), (36), and (87). The ratio of the sampling intervals and, as well, the ratio of the discretization intervals, equal the boson mass

$$m = \frac{K}{F} = \frac{\Delta_\kappa}{\Delta_\varphi}. \tag{89}$$

By definition, the optimal boson mass requires the minimal number of the discretization points for an accurate representation. In principle, for a specified accuracy, the optimal boson mass can be obtained by minimizing the cutoff N_b of the wave function's expansion in the boson number basis. However, this is not easy to accomplish, since the extraction of N_b from quantum simulations is laborious, as will be discussed in Sec. V.

Nevertheless, instead of finding the boson mass for optimal representation, one can ask about the boson mass that yields optimal sampling. Adjusting parameters for optimal sampling in quantum simulations is much easier than optimizing for the smallest cutoff N_b, as will be discussed in Sec. V. The sampling accuracy of a wave function is determined by the wave function behavior outside the field and the conjugate-field sampling intervals. For a specified accuracy ϵ, the sampling intervals parameters F and K should be chosen such that [see Eqs. (8) and (11)]

$$\|w^\phi_F\| = \|w^\phi_K\| = \epsilon. \tag{90}$$

This choice will provide, via Eq. (15), the minimum number of discretization points required for a sampling approximation with $O(\epsilon)$ accuracy.

Do the sampling intervals F and K determined by imposing Eq. (90) yield the optimal boson mass through Eq. (89)? While we do not know the answer in general, numerical checks show that the answer is *yes* in many cases. That is the case of the harmonic oscillator, as was already discussed in Sec. IV A. We also found the answer to be *yes* for small size Φ^4 scalar field models that we can solve numerically using exact diagonalization methods. In the following, we present two relevant Φ^4 scalar field examples.

1. Local Φ^4 scalar field

The first example is a strong interacting local Φ^4 field model, equivalent to an anharmonic oscillator, with the Hamiltonian

$$H = \frac{\Pi^2}{2} + \frac{1}{2}m_0^2\Phi^2 + \frac{g}{4!}\Phi^4. \tag{91}$$

Figure 8(a) shows the field and the conjugate-field distribution of the ground state of the Hamiltonian (91) for interaction strength $\frac{g}{m_0^3} = 100$. One effect of the interaction is to narrow the field distribution $|\Phi(\varphi)|^2$ and to widen the conjugate-field distribution $|\hat{\Phi}(\kappa)|^2$ compared to the noninteracting case. The

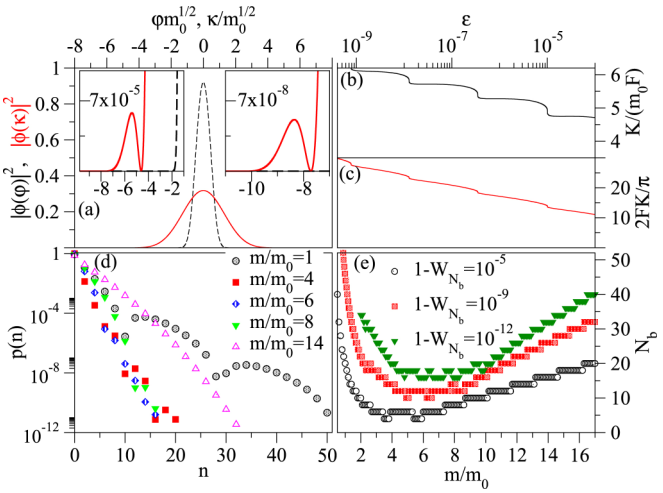

FIG. 8. Local ϕ^4 field theory, Eq. (91), with $\frac{g}{m_0^3} = 100$. (a) Field and conjugate-field distributions, $|\Phi(\varphi)|^2$ (dashed black) and $|\hat{\Phi}(\kappa)|^2$ (solid red), respectively, in the ground state. Insets: The conjugate-field distribution has an oscillatory behavior at large $|\kappa|$. (b) The ratio of the sampling intervals widths $\frac{K}{F}$ vs the tail weight ϵ, calculated by employing Eq. (90). $\frac{K}{F}$ is larger than the bare mass m_0, and increases logarithmically with increasing the accuracy. (c) The number of the required discretization points $N_\varphi = \lceil \frac{2}{\pi} FK \rceil$ increases logarithmically with decreasing the tail weight. (d) m-boson distribution for different choices of $\frac{m}{m_0}$. (e) The low-energy subspace cutoff N_b vs $\frac{m}{m_0}$ for different truncation errors $1 - W_{N_b}$. The optimal boson mass is found when N_b is minimum.

interaction also affects the field distributions behavior at large argument, as can be seen in the insets. The wave function $\hat{\Phi}(\kappa)$ has an oscillatory behavior at large $|\kappa|$.

Optimal sampling implies a ratio ($\propto K/F$) larger than the bare mass m_0, because the $|\hat{\Phi}(\kappa)|^2$ distribution is wider than the $|\Phi(\varphi)|^2$ one. Figure 8(b) shows the ratio of the sampling intervals $\frac{1}{m_0}\frac{K}{F}$ vs the tail weight ϵ, where F and K are determined by Eq. (90). The ratio $\frac{1}{m_0}\frac{K}{F}$ is dependent on ϵ, and increases logarithmically (and nonuniformly due to the oscillatory behavior of $|\hat{\Phi}(\kappa)|^2$) with increasing the accuracy, from $\frac{1}{m_0}\frac{K}{F} \approx 4$ for an accuracy $\epsilon = 10^{-3}$ to $\frac{1}{m_0}\frac{K}{F} \approx 6$ for $\epsilon = 10^{-9}$. The number of discretization points $N_\varphi = \lceil 2KF/\pi \rceil$, necessary to sample the local Φ^4 field ground state increases logarithmically with increasing the accuracy, as can be seen in Fig. 8(c).

To calculate the boson distribution, we diagonalize numerically the Hamiltonian (91) in the boson number basis. Figure 8(d) shows the boson distribution, $p(n)$, as function of n for different choices of the boson mass. In all cases, the boson distribution decreases rapidly with increasing number of bosons. We find that the largest decreasing slope occurs when the boson mass $m/m_0 \in \approx [4, 8]$. Figure 8(e) shows the cutoff N_b vs the boson mass for different truncation errors $1 - W_{N_b}$. Remember that $1 - W_{N_b}$, with W_{N_b} defined by Eq. (75), is the weight of the subspace spanned by the boson number states above the cutoff. The optimal boson mass occurs at the minimum of $N_b(m/m_0)$. For a truncation error $1 - W_{N_b} \approx 10^{-5}$ we find $m/m_0 \approx 4$. The optimal boson mass increases to $m/m_0 \approx 8$ with decreasing the truncation error to $1 - W_{N_b} \approx 10^{-12}$.

The optimal boson mass determined by minimizing N_b is in agreement with the boson mass calculated by minimizing the sampling errors of $\Phi(\varphi)$ and $\hat{\Phi}(\kappa)$. Since the truncation error given by the weight of the subspace spanned by the boson number states above the cutoff is not the same as the sampling error determined by the wave function's weight outside the sampling intervals, a quantitative comparison between $\frac{K}{F}$ plotted in Fig. 8(b) and an optimal boson mass extracted from Fig. 8(e) is not meaningful. However, we found in both cases that the optimal boson mass is in the same range, $m/m_0 \in [4, 8]$, and that it increases when increasing the accuracy of the approximation.

2. *Two-site Φ^4 scalar field*

The next example is a two-site Φ^4 field theory,

$$H = \sum_{i=1,2} \left(\frac{\Pi_i^2}{2} + \frac{1}{2} m_0^2 \Phi_i^2 + \frac{g}{4!} \Phi_i^4 \right) - h \Phi_1 \Phi_2, \tag{92}$$

with $m_0^2 = -1$, $\frac{g}{|m_0|^3} = 2$ and $\frac{h}{|m_0|^2} = 1$. The coupling between the fields operators at neighboring sites is a consequence of the gradient term, $(\nabla\Phi)^2$, present in the Lagrangian of a continuous Φ^4 field theory. Although no real broken symmetry occurs for a two-site system, the negative value of m_0^2 yields interesting behavior relevant for exploring models with a broken symmetry phase. The field in the ground state has a two-peak structure and the excitation gap is small.

The local field distribution,

$$p_1(\varphi) = \langle \varphi | \rho_1 | \varphi \rangle, \tag{93}$$

and the local conjugate-field distribution,

$$p_1(\kappa) = \langle \kappa | \rho_1 | \kappa \rangle, \tag{94}$$

are plotted in Fig. 9(a). In Eqs. (93) and (94) ρ_1 is the local density matrix

$$\rho_1 = \mathrm{Tr}_2(|\phi\rangle\langle\phi|), \tag{95}$$

obtained by tracing out the degrees of freedom at site 2, while $|\phi\rangle$ in Eq. (95) is the ground state of the Hamiltonian (92).

Since the sampling errors of lattice wave functions depend on the tail weights of the local distributions (see Appendix B 2), the sampling intervals lengths are determined by imposing $w_{1F}^{\phi} = w_{1K}^{\phi} = \epsilon$, where

$$w_{1F}^{\phi\ 2} = \int_{-\infty}^{-F} d\varphi \langle \varphi | \rho_1 | \varphi \rangle + \int_{F}^{\infty} d\varphi \langle \varphi | \rho_1 | \varphi \rangle, \tag{96}$$

$$w_{1K}^{\phi\ 2} = \int_{-\infty}^{-K} \langle \kappa | \rho_1 | \kappa \rangle \, d\kappa + \int_{K}^{\infty} \langle \kappa | \rho_1 | \kappa \rangle \, d\kappa \tag{97}$$

[see also Eqs. (B28) and (B40)]. As can be seen in the inset of Fig. 9(a), the local field distribution decays more rapidly with increasing argument than the conjugate-field one. The ratio of the sampling intervals widths, $\frac{1}{|m_0|}\frac{K}{F}$, versus the tail weight is plotted in Fig. 9(b). It increases logarithmically with decreasing tail weight, from $\frac{1}{|m_0|}\frac{K}{F} \approx 1.2$ when the tail weight is $\epsilon \approx 10^{-4}$ to $\frac{1}{|m_0|}\frac{K}{F} \approx 2$ for a tail weight $\epsilon \approx 10^{-12}$.

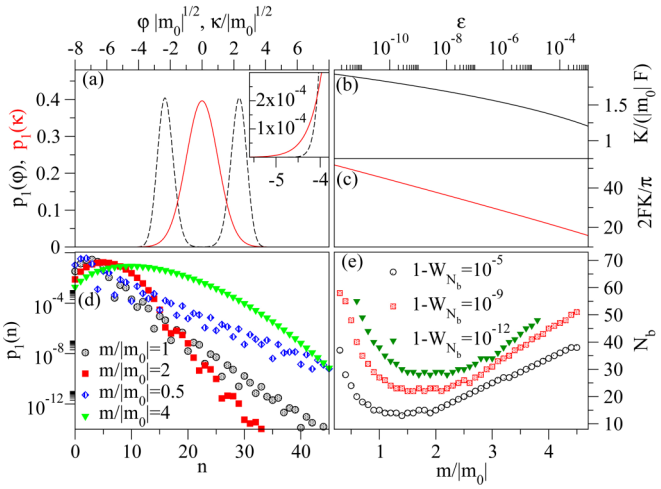

FIG. 9. Two-site Φ^4 field theory, Eq. (92), with $m_0^2 = -1$ and $\frac{g}{|m_0|^3} = 2$ and $h = 1$ (a) Local field, Eq. (93) (dashed black) and conjugate-field, Eq. (94) (continuous red) distributions in the ground state. Inset: At large argument, the field distribution decays faster than the conjugate-field distribution. (b) The ratio of the sampling intervals widths $\frac{K}{F}$ vs the tail weight. $\frac{K}{F}$ is larger than $|m_0|$ and increases logarithmically with increasing accuracy. (c) The number of required discretization points $N_\varphi = \lceil \frac{2}{\pi} FK \rceil$ increases logarithmically with decreasing the tail weight. (d) m-boson local distribution for different choices of $\frac{m}{|m_0|}$. (e) The low-energy subspace cutoff N_b vs $\frac{m}{|m_0|}$ for different truncation errors $1 - W_{N_b}$. The optimal boson mass is found when N_b is minimum.

The number of discretization points, $N_\varphi = \lceil \frac{2}{\pi} FK \rceil$, increases logarithmically with the accuracy, as shown in Fig. 9(c).

The local boson distribution,

$$p_1(n) = \langle n|\rho_1|n\rangle, \tag{98}$$

for different choices of the boson mass is shown in Fig. 9(d). The boson distribution decreases rapidly with increasing number of bosons. The largest decreasing slope is observed for $m/|m_0| \approx 2$. The cutoff N_b versus the boson mass is shown in Fig. 9(e) for different values of the truncation error $1 - W_{N_b}$. For a truncation error $1 - W_{N_b} \approx 10^{-5}$ we find the optimal boson mass to be $m/|m_0| \approx 1.2$. The optimal boson mass increases to $m/|m_0| \approx 2$ with decreasing the truncation error to $1 - W_{N_b} \approx 10^{-12}$.

As in the case of the local Φ^4 field example, the boson optimal mass calculated by minimizing N_b is in agreement with the boson mass that minimizes the sampling errors of the local field distributions $p_1(\varphi)$ and $p_1(\kappa)$. In both cases, the boson mass is in the same range, $m/|m_0| \in [1.2, 2]$, and it increases when increasing the accuracy of the approximation.

Note that the optimal mass from our analysis is not determined by the standard deviation of the field distributions but by the field and conjugate-field distributions' behavior at large argument. The ratio of the standard deviations in some mean-field theory approaches is related to the value of the boson mass. Our results suggest that the mean-field solutions obtained in this way are not very good approximations to the optimal mass.

V. POSTSIMULATION DISCRETIZATION VALIDATION AND PARAMETERS ADJUSTMENT

For an accurate simulation, the low-energy subspace should be large enough to contain the relevant physics. The number N_φ of discretization points per lattice site and the boson mass determine the low-energy subspace, but the optimal values for these parameters are not known *a priori*. Therefore, it is important to determine *a posteriori* whether the chosen simulation's parameters are good and to have procedures to adjust them for optimal performance.

Note that when sufficient quantum computational resources are available, in order to estimate the accuracy of the simulation's results, one can run simulations for subsequently increasing values of N_φ and analyze the results' convergence properties. However, this approach does not provide direct information about optimal discretization intervals and likely will result in suboptimal use of the available resources.

A. Local measurements

The results of a quantum simulation are obtained by measuring the state of the qubits in the computational basis. Not all information about the system is easily accessible from quantum simulations. To validate the choice of discretization parameters in our simulation, we only need measurements of the local field distribution, the local conjugate-field distribution and the local boson distribution. Fortunately, these observables can be measured relatively easily. We discuss their measurements below.

The implementation of quantum algorithms for bosonic fields is described at length in Refs. [6,7,19]. Here we present only the minimum information necessary to understand the measurements methods. For every lattice site, $n_q = \log_2(N_\varphi)$ qubits are assigned and the discrete field eigenvector $|\tilde{\varphi}_i\rangle_j$ is mapped to

$$|\tilde{\varphi}_i\rangle_j \equiv \left|x_0^i, \ldots, x_{n_q-1}^i\right\rangle_j, \tag{99}$$

where $x_r^i \in \{0, 1\}$ and $j = \overline{1, N}$ is the site label. The field operators [see Eqs. (40) and (65)] are defined by

$$\tilde{\Phi}_j|\tilde{\varphi}_i\rangle_j = \varphi_i|\tilde{\varphi}_i\rangle_j \quad \text{with} \quad \varphi_i = \Delta_\varphi\left(\sum_{r=0}^{n_q-1} 2^r x_r^i - \frac{N_\varphi - 1}{2}\right). \tag{100}$$

The field distribution at site j is given by

$$p_j(\varphi_i) = \langle\tilde{\varphi}_i|\rho_j|\tilde{\varphi}_i\rangle \tag{101}$$

and is obtained by the direct measurement of the qubits assigned to represent the field at site j, as shown in Fig. 10(a).

The conjugate-field distribution at site j is given by

$$p_j(\kappa_p) = \langle\tilde{\kappa}_p|\rho_j|\tilde{\kappa}_p\rangle, \tag{102}$$

where $\{|\tilde{\kappa}_p\rangle_j\}_p$ are obtained by applying a local Fourier transform (i.e., a n_q-qubit Fourier transform at site j) to $\{|\tilde{\varphi}_i\rangle_j\}_i$, as described by Eq. (43). The measurement of this distribution requires an inverse Fourier transform, $\tilde{\mathcal{F}}^{-1}$ [see Eq. (42)], at site j before measuring the qubits, as shown in Fig. 10(b).

The finite representation of the boson occupation number distribution (i.e., the probability of the discrete harmonic

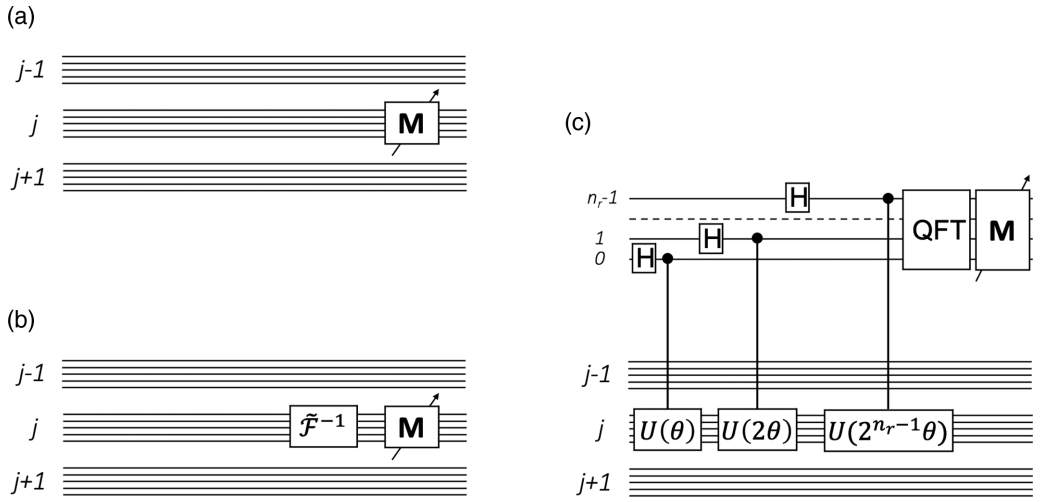

FIG. 10. At every lattice site $n_q = \log_2(N_\varphi)$ qubits are assigned to represent the field. (a) The field amplitude distribution at site j can is obtained by direct measurement of the qubits assigned for the site j. (b) The conjugate-field amplitude distribution requires an inverse Fourier transform, $\tilde{\mathcal{F}}^{-1}$ [see Eq. (42)] at j before measurement. (c) Quantum phase estimation algorithm for measuring the boson distribution at site j. An ancillary register of size $n_r = n_q + 1$ is used to store the phase factors associated with the evolution of the system under the action of a local discrete harmonic oscillator Hamiltonian [Eq. (109)].

oscillator eigenstates) at site j is given by

$$p_j(n) = \langle\tilde{\phi}_n|\rho_j|\tilde{\phi}_n\rangle. \tag{103}$$

If we write the system's wave function as

$$|\phi\rangle = \sum_e \sum_{n=0}^{N_\varphi-1} c_{en}|e\rangle|\tilde{\phi}_n\rangle_j, \tag{104}$$

where $\{|e\rangle\}$ is an arbitrary basis for the whole system with the site j excluded, the boson distribution is

$$p_j(n) = \sum_e |c_{en}|^2. \tag{105}$$

The probability to have bosons above the cutoff N_b is given by

$$\epsilon_H = \sum_{n=N_b}^{N_\varphi-1} p_j(n) = \sum_e \sum_{n=N_b}^{N_\varphi-1} |c_{en}|^2. \tag{106}$$

The bosonic field representation is accurate when ϵ_H is negligible.

We present two methods for the measurement of the local boson distribution. The first method employs quantum state tomography (QST) for the local density matrix ρ_j. As described in [12,13], ρ_j can be written as

$$\rho_j = \frac{1}{2^{n_q}} \sum_{v_0,\ldots,v_{n_q-1}=0}^{3} s_{v_0,\ldots,v_{n_q-1}} P_{v_0,\ldots,v_{n_q-1}}. \tag{107}$$

The *Pauli strings* $P_{v_0,\ldots,v_{n_q-1}} \equiv \sigma^j_{v_0} \otimes \sigma^j_{v_1} \otimes \cdots \otimes \sigma^j_{v_{n_q-1}}$ are products of Pauli matrices. The single-qubit operator $\sigma^j_{v_q}$, acting on the qubit $q \in \{0, 1, \ldots, n_q - 1\}$ belonging to the local register at site j, takes four possible values, $\sigma^j_{v_q} \in \{I, \sigma_x, \sigma_y, \sigma_z\}$. The coefficients $s_{v_0,\ldots,v_{n_q-1}} = \mathrm{Tr}(P_{v_0,\ldots,v_{n_q-1}}\rho_j)$ are determined by measuring the corresponding Pauli strings. Similar measurements of the Pauli strings are also employed in Variational Quantum Eigensolver algorithms [29]. Since the number of the independent coefficients defining ρ_j is $4^{n_q} - 1$, the number of measurements required for QST scales exponentially with n_q. This put a severe limitation on QST with large n_q [30–32]. However, the current experimental development [32–34] indicates that QST for $n_q \leqslant 8$ (which we believe is large enough for addressing most interesting boson problems) will be feasible in the near future.

Once the local density matrix is determined, its elements in the computational basis can be easily calculated, since this implies evaluating the matrix elements of the Pauli strings in the computational basis. Finally, the boson distribution is given by

$$p_j(n) = \sum_{i,l=0}^{N_\varphi-1} \langle\tilde{\phi}_n|\tilde{\varphi}_i\rangle\langle\tilde{\varphi}_i|\rho_j|\tilde{\varphi}_l\rangle\langle\tilde{\varphi}_l|\tilde{\phi}_n\rangle, \tag{108}$$

where the coefficients $\langle\tilde{\phi}_n|\tilde{\varphi}_i\rangle$ are obtained from the exact diagonalization of the discrete harmonic oscillator Hamiltonian (45).

The second method for the measurement of the boson distribution at the lattice site j employs quantum phase estimation (QPE) [13,14] measurements for the discrete harmonic oscillator

$$\tilde{H}_{h1} = \frac{1}{2}\tilde{\Pi}^2 + \frac{1}{2}m_0^2\tilde{\Phi}^2 - \frac{1}{2}m_0 = H_h - \frac{1}{2}m_0, \tag{109}$$

where we subtract the constant term $\frac{1}{2}m_0$ for convenience. The eigenvalues of the Hamiltonian (109) have the following property (within the desired accuracy of the finite representation approximation):

$$\tilde{E}_n = m_0 n, \quad \text{for} \quad n < N_b, \tag{110}$$

$$\tilde{E}_n \neq m_0 n, \quad \text{for} \quad n \geqslant N_b. \tag{111}$$

For example, see the eigenvalues of the discrete harmonic oscillator for $N_\varphi = 64$ and $N_\varphi = 128$ plotted in Fig. 1(a) of Ref. [7].

The time evolution operator corresponding to Hamiltonian (109)

$$U(\theta) \equiv e^{-i2\pi\theta H_{h1}} \tag{112}$$

can be implemented using Trotterization methods, as described in Refs. [6,7,19]. The operator (112) acts only on the n_q qubits assigned to the field at the site j.

The implementation of the phase estimation algorithm is illustrated in Fig. 10(c). An ancillary register of n_r qubits is used. On every ancillary qubit, a Hadamard gate is applied. Next, for every qubit m from the ancillary register (with $m = \overline{0, n_r - 1}$), a control-$U(2^m\theta)$ gate, acting on the ancilla qubit m and the local field register at site j, is applied.

The state of the system together with the ancillas changes from

$$|\phi\rangle|0\rangle_a = \sum_e \sum_{n=0}^{N_\varphi-1} c_{en}|e\rangle|\tilde{\phi}_n\rangle_j|0\rangle_a, \tag{113}$$

where $|0\rangle_a$ is the ancillary register state, to

$$\sum_e \sum_{n=0}^{N_\varphi-1} c_{en}|e\rangle|\tilde{\phi}_n\rangle_j \frac{1}{2^{\frac{n_r}{2}}} \sum_{x=0}^{2^{n_r}-1} |x\rangle_a e^{-i2\pi\theta\tilde{E}_n x}, \tag{114}$$

after applying the Hadamard and the CU operators. In Eq. (114), $|x\rangle_a$ is the binary representation on qubits of the integer $x = \overline{0, 2^{n_r} - 1}$. To distinguish between the phase factors corresponding to all eigenvalues of the Hamiltonian (109), the parameter θ should be chosen such that

$$\theta < \frac{1}{\Delta E}, \quad \text{where } \Delta E = \max_n \tilde{E}_n - \min_n \tilde{E}_n \tag{115}$$

is the range of the Hamiltonian (109) spectrum.

After the quantum Fourier transform is applied on the ancilla register, the state described previously by Eq. (114) becomes

$$|\chi\rangle \equiv \sum_e \sum_{n=0}^{N_\varphi-1} \sum_{k=0}^{2^{n_r}-1} c_{en}a_{nk}|e\rangle|\tilde{\phi}_n\rangle_j|k\rangle_a, \tag{116}$$

where $|k\rangle_a$ is the binary representation on qubits of the integer $k = \overline{0, 2^{n_r} - 1}$ and

$$a_{nk} = \frac{1}{2^{n_r}} \sum_{x=0}^{2^{n_r}-1} e^{-i\frac{2\pi}{2^{n_r}}(2^{n_r}\theta\tilde{E}_n - k)x}. \tag{117}$$

The probability to measure the integer k on the ancilla register is given by

$$p(k) = \sum_e \sum_{n=0}^{N_\varphi-1} |c_{en}a_{nk}|^2. \tag{118}$$

If we choose

$$\theta = \frac{1}{m_0 2^{n_r}}, \tag{119}$$

then

$$a_{nk} = \frac{1}{2^{n_r}} \sum_{x=0}^{2^{n_r}-1} e^{-i\frac{2\pi}{2^{n_r}}(\frac{\tilde{E}_n}{m_0} - k)x}. \tag{120}$$

The choice of θ given by Eq. (119) is convenient since $\tilde{E}_n/m_0 = n$ for $n < N_b$. Thus, for $n < N_b$ Eq. (117) is a Kronecker delta function, $a_{nk} = \delta_{nk}$. The probability to measure an integer $k \geqslant N_b$ in the ancilla register reduces to

$$p(k) = \sum_e \sum_{n=N_b}^{N_\varphi-1} |c_{en}|^2|a_{nk}|^2, \quad \text{for } k \geqslant N_b, \tag{121}$$

since the terms in Eq. (118) with $n < N_b$ are zero. Since $|a_{nk}| \leqslant 1$ (see Appendix E), we have the following inequality:

$$p(k) \leqslant \sum_e \sum_{n=N_b}^{N_\varphi-1} |c_{en}|^2 = \epsilon_H, \quad \text{for } k \geqslant N_b. \tag{122}$$

For any $k \geqslant N_b$, the probability to measure k is smaller than the probability to have more than N_b bosons. Thus

$$\epsilon_H \geqslant \max_{k\geqslant N_b} p(k) \equiv p_{1\max}. \tag{123}$$

The probability to measure any integer $k \geqslant N_b$ in the ancilla register is given by

$$\begin{aligned} p_{\text{all}} &= \sum_{k=N_b}^{2^{n_r}-1} p(k) = \sum_e \sum_{n=N_b}^{N_\varphi-1} |c_{en}|^2 \sum_{k=N_b}^{2^{n_r}-1} |a_{nk}|^2 \\ &\geqslant \frac{4}{\pi^2} \sum_e \sum_{n=N_b}^{N_\varphi-1} |c_{en}|^2 = \frac{4}{\pi^2}\epsilon_H. \end{aligned} \tag{124}$$

In Eq. (124), we used

$$\sum_{k=N_b}^{2^{n_r}-1} |a_{nk}|^2 \geqslant \max_{k\geqslant N_b} |a_{nk}|^2 \geqslant \frac{4}{\pi^2} \quad \text{for } n > N_b, \tag{125}$$

which is proven in Appendix E [see Eq. (E5)].

Combining Eq. (123) and Eq. (124), the probability to have more than N_b bosons is bounded as

$$p_{1\max} \leqslant \epsilon_H \leqslant \frac{\pi^2}{4} p_{\text{all}}. \tag{126}$$

According to Eq. (126), the discretization parameters N_φ and m_0 used for bosonic field representation are valid if there is a negligible probability to measure integers larger than the cutoff $N_b(N_\varphi)$ on the ancillary registry.

The size of the ancillary register is determined by Eq. (115) and Eq. (119),

$$n_r \geqslant \log_2\left(\left[\frac{\Delta E}{m_0}\right]\right). \tag{127}$$

The number of ancillary qubits scales logarithmically with the energy range of the discrete harmonic oscillator Hamiltonian. The values of the energy range ΔE corresponding to different N_φ are given in Table I. We find that $\Delta E/m_0 < 2N_\varphi$ for $N_\varphi \leqslant 1024$ (and probably true for larger values of N_φ as well but numerical checks are necessary for confirmation). In practice the number of ancillary qubits required for the QPE register is

$$n_r = n_q + 1. \tag{128}$$

Measuring energies in QPE algorithms with 2^{-n} accuracy and with $1 - \epsilon$ probability requires registers of size $n_r = n + \log_2[2 + 1/(2\epsilon)]$ [13,14], thus larger than in our case

TABLE I. Middle row: Energy range of the discrete harmonic oscillator for different values of N_φ, calculated using exact diagonalization. Bottom row: Boson cutoff number corresponding to the commutation relation error [Eq. (58)] $\epsilon_c \approx 10^{-4}$.

N_φ	32	64	128	256	512	1024
$\Delta E/m_0$	42.319	89.396	185.376	379.976	772.944	1564.233
N_b ($\epsilon_c < 10^{-4}$)	10	30	74	164	353	741

when $\epsilon \lesssim 10^{-2}$. In our case, the goal of the QPE measurement is not to estimate the energies of H_h (which we know from exact diagonalization of the finite Hamiltonian matrix) but to measure the boson distribution and especially the probability to have states with the number of bosons larger than N_b. When the probability to have bosons above the cutoff is negligible, i.e., $\epsilon_H \approx 0$, the boson distribution can be measured with high precision. This is true because the energies of the states with $n < N_b$ are proportional to n [see Eq. (110)], Eq. (120) becomes a Kronecker delta function and the probability to measure $k < N_b$ on the ancillary register becomes equal to the probability to have n bosons [see Eq. (105)],

$$p(k=n) = \sum_e |c_{en}|^2 = p_j(n) \quad \text{for} \quad k < N_b \quad \text{when} \quad \epsilon_H = 0. \tag{129}$$

B. Simulation guideline for parameters' validation and adjustment

In this section, we present a guideline for quantum simulations of bosonic fields. The main goal is to provide a practical procedure for adjusting N_φ and boson mass m for optimal performance. Let's assume for now that the system has translational symmetry and the local measurements yield identical results at all sites:

(1) If 10 or less bosons per site is expected to be adequate to capture the low-energy physics, start with $N_\varphi = 32$ discretization points per lattice site. Otherwise start with a larger N_φ. Equation (61) can be used to determine the dependence $N_b(N_\varphi, \epsilon)$. In Table I we provide the value of N_b for different N_φ when the accuracy is of order $O(10^{-4})$.

(2) Start with a boson mass $m = m_0 + \delta m$, where m_0 is the bare mass and δm is the mean-field contribution.

(3) After the system state is prepared on qubits, measure the local field distribution, $p_j(\varphi_i)$, and the conjugate-field distribution, $p_j(\kappa_p)$ at the arbitrary site j, as described in Sec. V A.

(4) Determine the coefficients β_φ and β_κ such that the probability to measure the field outside the range $[-\beta_\varphi F, \beta_\varphi F]$ and the probability to measure the conjugate field outside the range $[-\beta_\kappa K, \beta_\kappa K]$, respectively, is smaller than ϵ,

$$\sum_{i \text{ for } |\varphi_i| > \beta_\varphi F} p_j(\varphi_i) < \epsilon, \tag{130}$$

$$\sum_{p \text{ for } |\kappa_p| > \beta_\kappa K} p_j(\kappa_p) < \epsilon. \tag{131}$$

If both $\beta_\varphi \leqslant f_c$ and $\beta_\kappa \leqslant f_c$ the wave function sampling is accurate. The parameter $0 < f_c < 1$ should be chosen to ensure confidence that the distribution weights at large argument are ϵ small. When f_c is very large the confidence is low and when f_c is very small resources are wasted. We believe that an acceptable range value for f_c is [0.6, 0.8].

The factors β_φ and β_κ can be modified by changing the mass factor since they depend on the intervals' widths $F \propto m^{-1/2}$ and $K \propto m^{1/2}$ [see Eq. (87)]. A change of the boson mass by a factor μ, $m \to \mu m$, implies $\beta_\varphi \to \sqrt{\mu}\beta_\varphi$ and $\beta_\kappa \to (1/\sqrt{\mu})\beta_\kappa$.

(5) If $\beta_\varphi \beta_\kappa \leqslant f_c^2$ and $\beta_\varphi \approx \beta_\kappa$ the guess of the initial mass was close to optimal. If $\beta_\varphi \beta_\kappa \leqslant f_c^2$ and $\beta_\varphi \not\approx \beta_\kappa$ adjust the boson mass by multiplying it with a factor of $\mu = \beta_\kappa/\beta_\varphi$. The new boson mass determines the optimal sampling discretization intervals.

(6) The case $\beta_\varphi \beta_\kappa > f_c^2$ means that both the field and the conjugate-field distributions close to the sampling intervals' edges are significant and cannot be adjusted properly by increasing one sampling interval and decreasing the other via boson mass scaling. The number N_φ of the discretization points should be increased by at least a factor of $\beta_\varphi \beta_\kappa / f_c^2$.

At this point the parameters N_φ and m are good for optimal field sampling. However, as shown in Sec. III C, accurate field sampling does not necessary implies wave function containment to the low-energy subspace.

(7) Measure the local boson distribution as described in Sec. V A.

(8) If the probability to measure integers $k \geqslant N_b$ are larger than ϵ, increase N_φ [and implicitly $N_b(N_\varphi, \epsilon)$] until the probability to measure integers $k \geqslant N_b$ are smaller than ϵ.

At this point the finite representation of the bosonic field defined by the parameters N_φ and m should be close to optimal for an accuracy $O(\epsilon)$.

In case the wave function has no translational symmetry, measurements at all sites are necessary for the validation and adjustment of the discretization parameters. The parameters N_φ and m should be chosen to provide accurate sampling and a boson distribution contained to the low-energy subspace at all sites. In this case, the global optimal m might not be optimal at every site.

In many simulations, the system's wave function changes in time under the action of the evolution operators. This might be the case for adiabatic continuation or for studying nonequilibrium physics, for example. In principle, measurements for the validation of the discretization parameters should be taken at every time step to make sure that the number of bosons above the cutoff is always smaller than ϵ. However, in practice, it is not necessary to take discretization validation measurements at every Trotter step. The effect of one Trotter step is of the order of the step size and, therefore, is small. Likely, it will be sufficient to take discretization validation measurements at a rather small number of time points, as long as the boson distribution is well below N_b for these measurements.

Use of the optimal parameters will yield the highest precision results for the computational resources available, but this can be challenging in practice. However, accurate, error-controlled quantum simulations can still be performed without adjusting the parameters to their optimal value as long as the problem we address can be restricted to the low-energy subspace. Adjusting the boson mass to the one optimizing the

sampling of the wave function might increase the precision of the simulations even when the mass is not optimal.

VI. DISCUSSION OF FUTURE APPLICATIONS

In this paper, we used the boson number basis to construct a local finite Hilbert space. A low-energy subspace was defined by introducing a cutoff in this basis. A different denumerable basis, for example $\{|\alpha_n\rangle\}$, might be considered for constructing a finite representation, following a similar procedure. However, this change is not trivial and would require the investigation of the Nyquist-Shannon sampling properties of $\langle\varphi|\alpha_n\rangle$ and $\langle\kappa|\alpha_n\rangle$, knowledge of the recurrence relations for $\varphi\langle\varphi|\alpha_n\rangle$ and $\kappa\langle\kappa|\alpha_n\rangle$ [similar to the ones given by Eq. (26) and Eq. (27), respectively] and measurement methods for the local distribution $\langle\alpha_n|\rho_j|\alpha_n\rangle$. We mention this as a topic for future investigation.

Quantum mechanical problems written in the *first quantization* formalism can be simulated on a quantum computer by employing the discretization methods developed for the bosonic fields. The position X_j and the momentum P_j operators (here j is an arbitrary label) entering the first quantization Hamiltonian $H(X_1, X_2, \ldots, P_1, P_2, \ldots)$ play the same role as the field operators Φ and Π, since they obey the canonical commutation relation $[X_j, P_l] = iI\delta_{jl}$. The field variable φ becomes the position variable x while the conjugate-field variable κ becomes the momentum variable p. The system's wave function is discretized in the position and momentum bases. For a general interaction potential $V(X_1, X_2, \ldots)$, a qubit implementation of the corresponding Trotter step operator requires the calculation of the phase factor proportional to $V(x_1, x_2, \ldots)$ for each qubit configuration $|x_1, x_2, \ldots\rangle$. This can be challenging when the computation resources are finite, being of similar difficulty as designing a quantum circuit to calculate the function $V(x_1, x_2, \ldots)$ [35,36]. However, when the potential can be approximated by a truncated Taylor expansion, the implementation reduces to a number of Trotter steps for the monomial terms appearing in the expansion. The Trotter step corresponding to a monomial term with degree r (for example $X_iX_{i+1}\cdots X_{i+r}$) requires $O(n_q^r)$ two-qubit gates [7]. Special care should also be taken to ensure that the number of the discretization points is large enough such that the action of $V(X_1, X_2, \ldots)$ does not violate the low-energy subspace constraints.

As for many quantum algorithms, the main limitation for the implementation of bosonic quantum algorithms on present-day quantum hardware is the two-qubit gate fidelity. Finite coherence time and control error restrict the maximum number of two-qubit gates to be less than 100 for quantum simulation algorithms implemented on state-of-art quantum processors [37,38]. This is not adequate for large bosonic field simulations, considering that a Trotter step requires $N \times 50 \sim N \times 10\,000$ two-qubit gates, where N is the lattice size (depending on the interaction type and strength). Problems which require time evolution simulations with thousands or millions of Trotter steps can probably be addressed only after error-corrected quantum technology is developed. However we are optimistic that interesting problems, such as the one-dimensional ϕ^4 model and polaron and bipolaron models, can be addressed on near-future quantum computers that can run circuits with thousands of two-qubit gates. For example, for problems where the cutoff $N_b \leqslant 10$ and the accuracy is $\epsilon \approx 10^{-2}$, we estimate Trotter steps requiring $N \times 50 \sim N \times 100$ two-qubits gates. These problems can be simulated on near-future hardware by employing noise mitigation techniques [39,40] and variational algorithms which only require the implementation of a few Trotter steps [41,42].

VII. CONCLUSIONS

In this work, we address the representation of lattice bosonic fields on the finite Hilbert space of quantum computers. An accurate representation (1) implies accurate storage of the wave function on qubits and (2) requires definition of qubit field operators whose action on the qubit wave function reproduces the action of the real field operators. We construct a finite representation for the low-energy subspace spanned by states with the number of bosons per site below a cutoff N_b. Since the lattice Hilbert space is a direct product of local Hilbert spaces, the representation of the lattice Hilbert space is a direct product of local Hilbert space representations.

A local Hilbert space is infinite dimensional and equivalent to the space of the square integrable functions. The construction of the finite representation for a local Hilbert space is based on Nyquist-Shannon sampling properties of square integrable functions. Because the weight of these functions vanishes at large argument, they can be sampled with controlled accuracy both in a finite set of field variable points and in a finite set of conjugate-field variable points. Within the same level of accuracy as the sampling approximation, the two sampling sets, of field and of conjugate-field points, are connected by a finite Fourier transform. The accuracy of the sampling approximation is determined by the weight of the functions outside the sampling intervals. The errors decrease with increasing the width of the sampling intervals and vanish in the infinite width limit.

By exploiting the sampling properties of the Hermite-Gauss functions, we construct a finite Hilbert space of dimension N_φ and define discrete field operators $\tilde{\Phi}$ and $\tilde{\Pi}$ such that, within $O(\epsilon)$ accuracy, the operators $\tilde{\Phi}$ and $\tilde{\Pi}$ act on the subspace spanned by the first $N_b < N_\varphi$ eigenstates of the discrete harmonic oscillator in the same way the field operators, Φ and Π, respectively, act on the subspace spanned by the first N_b harmonic oscillator eigenvectors. As long as the relevant physics of the system is restricted to the low-energy subspace defined by the cutoff N_b, the low-energy subspace can be mapped to the low-energy subspace of the finite Hilbert space.

We investigate analytically and numerically the different errors associated with the sampling of the HG functions and with the action of the discrete field operators on the eigenstates of the discrete harmonic oscillator. These errors are proportional to the tail weight of the HG functions. The accuracy of the finite representation is of the same order as the weight of the HG function of the order $N_b + 2$ outside the sampling interval. The errors are reduced exponentially by increasing the number of the discretization points. For fixed accuracy, the number of discretization points increases linearly with the size N_b of the low-energy subspace.

The definition of the finite Hilbert space and of the discrete field operators depends on the boson mass. The optimal boson

mass is the one that requires the smallest number of discretization points for a given accuracy. While a calculation of the optimal boson mass by minimizing the low-energy cutoff N_b is difficult in quantum simulations, finding a boson mass that minimizes the sampling errors of the system wave function is much easier. The boson mass optimizing the wave function's sampling equals the ratio of the sampling intervals that yield ϵ small tail weights. For scalar Φ^4 models on small lattices, we find that the boson mass optimizing the sampling is a good approximation for the optimal boson mass.

The states belonging to the low-energy subspace are sampled accurately. However, the converse is not true: accurate sampling does not necessarily imply that the states belong to the low-energy subspace. We present two examples of functions that are sampled with high accuracy but have a significant high-energy component. As a consequence, local boson distribution measurements are necessary to validate the discretization parameters of a quantum simulation.

We present a guideline to validate and adjust the discretization parameters N_φ and m that determine the accuracy of the simulation for optimal performance. The guideline requires measurements of the local field, local conjugate-field and local boson distributions. The field and conjugate-field measurements are done by measuring the qubits assigned to represent the field. For the measurement of the local boson distribution we present two methods. The first employs quantum state tomography of the n_q-qubit register assigned to describe the boson field at a particular lattice site. The second method employs the QPE technique for a discrete harmonic oscillator evolution operator acting on the local n_q qubit register. The QPE measurements require an ancillary register of size $n_q + 1$. The probability to measure bosons states above the cutoff is bounded by the probability to measure integers above the cutoff in the ancillary register. When the bosons number states above the cutoff have negligible weight, the local boson distribution can be measured with high precision. The guideline's first part explains how, based on the field and conjugate-field distribution measurements, the discretization parameters can be optimized for optimal sampling. The validation of the discretization parameters is finally done by measuring the local boson distribution. The parameters are valid if the probability to measure bosons above the cutoff is negligible. Otherwise the number of the discretization points should be increased.

The methodology presented here can be applied to quantum problems written in the first quantization formalism, since the position and momentum operators obey the same commutation relation as the field and conjugate-field operators.

The idea of using an interaction-dependent boson mass to represent the system's relevant degrees of freedom in the most efficient way is not new. When the optimal mass is used, the state of the system has the smallest number of excitations per site above the boson vacuum. This might be related to the renormalization theory method of using an interaction-dependent physical mass in the diagrammatic calculations. Instead of the bare mass, which has no real physical significance, the physical mass absorbs many divergent diagrams from the diagrammatic expansion. In our case, a large number of bosonic excitations are absorbed by redefining the boson mass.

ACKNOWLEDGMENTS

A.M. is partially supported by the DOE/HEP QuantISED program grant of the theory consortium "Intersections of QIS and Theoretical Particle Physics" at Fermilab. A.C.Y.L. and S.M. are partially supported by the DOE/HEP QuantISED program grant "HEP Machine Learning and Optimization Go Quantum," identification number 0000240323. This manuscript has been authored by Fermi Research Alliance, LLC under Contract No. DE-AC02-07CH11359 with the U.S. Department of Energy, Office of Science, Office of High Energy Physics.

APPENDIX A: NYQUIST-SHANNON SAMPLING WITH HALF-INTEGER SUMMATION INDICES

Let $f(\varphi)$ be a band-limited function, i.e., $\hat{f}(\kappa) = 0$ for $|\kappa| > K$, where $\hat{f}(\kappa)$ is the Fourier transform of $f(\varphi)$ defined by Eq. (5) and K is a positive real number.

The antiperiodicity of the function defined as

$$\hat{f}_{ap}(\kappa) = \hat{f}(\kappa) \text{ for } \kappa \in [-K, K], \tag{A1}$$

$$\hat{f}_{ap}(\kappa + 2K) = -\hat{f}_{ap}(\kappa) \tag{A2}$$

implies

$$\hat{f}_{ap}(\kappa) = \frac{\Delta_\varphi}{\sqrt{2\pi}} \sum_{i=-\infty}^{\infty} f(\varphi_i) e^{-i\kappa\varphi_i}, \quad \text{with}$$

$$\varphi_i = \left(i + \frac{1}{2}\right)\frac{\pi}{K} = \left(i + \frac{1}{2}\right)\Delta_\varphi, \tag{A3}$$

$$f(\varphi_i) = \frac{1}{\sqrt{2\pi}} \int_{-K}^{K} \hat{f}_{ap}(\kappa) e^{i\kappa\varphi_i}\, d\kappa. \tag{A4}$$

Since $\hat{f}(\kappa)$ has support only on the interval $[-K, K]$, it can be written as

$$\hat{f}(\kappa) = \hat{f}_{ap}(\kappa) R_K(\kappa), \tag{A5}$$

where $R_K(\kappa)$ is the rectangular function defined as

$$R_K(\kappa) = \begin{cases} 1 & \text{for } \kappa \in [-K, K] \\ 0 & \text{for } |\kappa| > K \end{cases}. \tag{A6}$$

The Fourier transforms of $R_K(\kappa)$ is proportional to the sinc function $u_K(\varphi)$ [see Eq. (13)],

$$\frac{1}{\sqrt{2\pi}} \int_{-K}^{K} e^{i\kappa\varphi}\, d\kappa = \sqrt{2\pi}\frac{\sin L\varphi}{\pi\varphi} = \frac{\sqrt{2\pi}}{\Delta_\varphi} \operatorname{sinc}\left(\frac{\varphi}{\Delta_\varphi}\right) \equiv \frac{\sqrt{2\pi}}{\Delta_\varphi} u_K(\varphi). \tag{A7}$$

The function $f(\varphi)$ is obtained by performing an inverse Fourier transform of Eq. (A5),

$$f(\varphi) = \frac{1}{\sqrt{2\pi}} \int_{-\infty}^{\infty} d\kappa e^{i\kappa\varphi} \frac{\Delta_\varphi}{\sqrt{2\pi}} \sum_{i=-\infty}^{\infty} f(\varphi_i) e^{-i\kappa\varphi_i} R_K(k)$$

$$= \sum_{i=-\infty}^{\infty} f(\varphi_i) u_K(\varphi - \varphi_i). \tag{A8}$$

Any band-limited function can be reconstructed from its values on an infinite and discrete set of sampling points, $\{\varphi_i = (i + \frac{1}{2})\Delta_\varphi\}_{i=\overline{-\infty,\infty}}$.

APPENDIX B: SAMPLING ERROR

1. Local wave functions

Consider the function $f(\varphi) \in S(\mathbb{R})$. The difference between $f(\varphi)$ and $\tilde{f}_\varphi(\varphi)$ defined by Eq. (14) is

$$\begin{aligned} f(\varphi) - \tilde{f}_\varphi(\varphi) &= f(\varphi) - \sum_{i=-\infty}^{\infty} f(\varphi_i) u_K(\varphi - \varphi_i) \\ &\quad + \sum_{|i|>\frac{N_\varphi-1}{2}} f(\varphi_i) u_K(\varphi - \varphi_i) \\ &= f(\varphi) - \langle\varphi|P_K|f\rangle + \sum_{i=-\infty}^{\infty} (\langle\varphi_i|P_K|f\rangle \\ &\quad - f(\varphi_i)) u_K(\varphi - \varphi_i) \\ &\quad + \sum_{i=-\infty}^{\infty} w_F^f(\varphi_i) u_K(\varphi - \varphi_i) \\ &= w_K^f(\varphi) - \sum_{i=-\infty}^{\infty} w_K^f(\varphi_i) u_K(\varphi - \varphi_i) \\ &\quad + \sum_{i=-\infty}^{\infty} w_F^f(\varphi_i) u_K(\varphi - \varphi_i), \end{aligned} \tag{B1}$$

where w_F^f and w_K^f were defined by Eq. (7) and Eq. (10), respectively. In the second line of Eq. (B1), we added and subtracted the band-limited term $\langle\varphi|P_K|f\rangle$.

Equaton (B1) can be written as

$$|f\rangle - |\tilde{f}_\varphi\rangle = |w_K^f\rangle - |v\rangle + |t\rangle \tag{B2}$$

with

$$\langle\varphi|v\rangle = \sum_{i=-\infty}^{\infty} w_K^f(\varphi_i) u_K(\varphi - \varphi_i), \tag{B3}$$

$$\langle\varphi|t\rangle = \sum_{i=-\infty}^{\infty} w_F^f(\varphi_i) u_K(\varphi - \varphi_i). \tag{B4}$$

The sampling error is bounded as

$$\|f - \tilde{f}_\varphi\| \leqslant \|w_K^f\| + \|v\| + \|t\|. \tag{B5}$$

To estimate $\|v\|$, we write $|v\rangle$ in the conjugate-field basis. Using Eq. (A7), we have

$$\begin{aligned} v(\kappa) &= \sum_{i=-\infty}^{\infty} w_K^f(\varphi_i) \frac{\Delta_\varphi}{\sqrt{2\pi}} R_K(\kappa) e^{-i\kappa\varphi_i} \\ &= \frac{1}{2K} \int dq w_K^f(q) R_K(\kappa) \sum_{i=-\infty}^{\infty} e^{i(q-\kappa)\varphi_i} \\ &= \sum_{n=-\infty}^{\infty} \int dq w_K^f(q) R_K(\kappa) (-1)^n \delta(\kappa - q + 2nK) \\ &= R_K(\kappa) \sum_{n=-\infty}^{\infty} (-1)^n w_K^f(\kappa + 2nK). \end{aligned} \tag{B6}$$

The $(-1)^n$ factor is a consequence of the half-integer values of the summation index i in Eq. (B6).

The vector $v(\kappa)$ can be written as

$$v(\kappa) = \sum_{n=-\infty}^{\infty} v_n(\kappa), \tag{B7}$$

where

$$v_n(\kappa) = R(\kappa)(-1)^n w_K^f(\kappa + 2nK). \tag{B8}$$

Note that $v_0(\kappa) = R(\kappa) w_K^f(\kappa) = 0$, since $w_K^f(\kappa) = \langle\kappa|Q_K|f\rangle = 0$ for $\kappa \in [-K, K]$.

For $n \neq 0$

$$\|v_n\|^2 = \int_{-K}^{K} \left|w_K^f(\kappa + 2nK)\right|^2 d\kappa = \int_{2nK-K}^{2nK+K} \left|w_K^f(\kappa)\right|^2 d\kappa. \tag{B9}$$

Now consider the function $\kappa\hat{f}(\kappa)$. Since $\hat{f}(\kappa) \in S(\mathbb{R}) \Rightarrow \kappa\hat{f}(\kappa) \in S(\mathbb{R})$. The tail weight of $\kappa\hat{f}(\kappa)$ outside the interval $[-K, K]$, denoted by r_K^f is

$$\left(r_K^f\right)^2 = \int_{-\infty}^{\infty} \kappa^2 \left|w_K^f(\kappa)\right|^2 d\kappa = \sum_{n=-\infty}^{\infty} \int_{2nK-K}^{2nK+K} \kappa^2 \left|w_K^f(\kappa)\right|^2 d\kappa. \tag{B10}$$

Since $k^2 \geqslant K^2 c^2(n)$ for $k \in [2nK - K, 2nK + K]$ and

$$c(n) = \begin{cases} 2n - 1 & \text{for} \quad n > 0 \\ 2n + 1 & \text{for} \quad n < 0 \end{cases}, \tag{B11}$$

the following inequality is true:

$$\begin{aligned} \left(r_K^f\right)^2 &\geqslant K^2 \sum_{n=-\infty}^{\infty} c(n)^2 \int_{2nK-K}^{2nK+K} \left|w_K^f(\kappa)\right|^2 \\ &= K^2 \sum_{n=-\infty}^{\infty} c(n)^2 \|v_n\|^2. \end{aligned} \tag{B12}$$

Employing Eq. (B7), the Cauchy-Schwartz inequality and Eq. (B12), one gets

$$\begin{aligned} \|v\| &\leqslant \sum_{n\neq 0} \|v_n\| |c(n)| \frac{1}{|c(n)|} \\ &\leqslant \sqrt{\sum_{n\neq 0} c(n)^2 ||v_n||^2} \sqrt{\sum_{n\neq 0} \frac{1}{c(n)^2}} \\ &= \frac{\pi}{2} \sqrt{\sum_{n\neq 0} c(n)^2 ||v_n||^2} \leqslant \frac{\pi r_K^f}{2K}. \end{aligned} \tag{B13}$$

In Eq. (B13) we used

$$\sum_{n\neq 0} \frac{1}{c(n)^2} = 2 \sum_{n>1} \frac{1}{(2n-1)^2} = \frac{\pi^2}{4}. \tag{B14}$$

The square norm $\|t\|^2$ is given by

$$\|t\|^2 = \int_{-\infty}^{\infty} d\varphi \sum_{i,j=-\infty}^{\infty} w_F^f(\varphi_i)^* w_F^f(\varphi_j) \times \int_{-\infty}^{\infty} u_K(\varphi-\varphi_i)u_K(\varphi-\varphi_j)\,d\varphi = \Delta_\varphi \sum_{i=-\infty}^{\infty} \left|w_F^f(\varphi_i)\right|^2. \tag{B15}$$

Note that the sum over i in Eq. (B15) is just the Riemann approximation of the integral $\int |w_F^f(\varphi)|^2\,d\varphi$. Using the Euler-Maclaurin integration rule [43], one gets the following approximation:

$$\|t\|^2 \approx \left\|w_F^f\right\|^2 + \frac{\Delta_\varphi}{2}\left(|f(-F)|^2 + |f(F)|^2\right) + O\left(\Delta_\varphi^2\right). \tag{B16}$$

Equations (B5), (B13), and (B16) imply

$$\|f - \tilde{f}_\varphi\| \lesssim \left\|w_K^f\right\| + \left\|w_F^f\right\| + \frac{\pi r_K^f}{2K} + \sqrt{\frac{\pi}{2K}[|f(-F)|^2 + |f(F)|^2]}. \tag{B17}$$

2. Lattice wave functions

For a wave function $f(\boldsymbol{\varphi}) \equiv f(\varphi_1, \varphi_2, \ldots, \varphi_N) \in S(\mathbb{R}^N)$, let's consider a sampling interval $[-\boldsymbol{F}, \boldsymbol{F}] \equiv [-F, F]^N \subset \mathbb{R}^N$, the projector

$$P_{\boldsymbol{F}} = \int_{-F}^{F} \cdots \int_{-F}^{F} |\boldsymbol{\varphi}\rangle\langle\boldsymbol{\varphi}| d\boldsymbol{\varphi} \tag{B18}$$

and the tail vector

$$\left|w_{\boldsymbol{F}}^f\right\rangle = (1 - P_{\boldsymbol{F}})|f\rangle \equiv Q_{\boldsymbol{F}}|f\rangle. \tag{B19}$$

Analogously, for the conjugate-field function $\hat{f}(\boldsymbol{\kappa}) \equiv \hat{f}(\kappa_1, \kappa_2, \ldots, \kappa_N) \in S(\mathbb{R}^N)$ let's consider the sampling interval $[-\boldsymbol{K}, \boldsymbol{K}] \equiv [-K, K]^N \subset \mathbb{R}^N$, the projector

$$P_{\boldsymbol{K}} = \int_{-K}^{K} \cdots \int_{-K}^{K} |\boldsymbol{\kappa}\rangle\langle\boldsymbol{\kappa}| d\boldsymbol{\kappa} \tag{B20}$$

and the tail vector

$$\left|w_{\boldsymbol{K}}^f\right\rangle = (1 - P_{\boldsymbol{K}})|f\rangle \equiv Q_{\boldsymbol{K}}|f\rangle. \tag{B21}$$

As for the one-dimensional functions, when K is large $|f\rangle \approx P_{\boldsymbol{K}}|f\rangle$, the Nyquist-Shannon theorem can be employed and $f(\boldsymbol{\varphi})$ can be approximated by a infinite series expansion of sinc functions products. When F is large, the series can be truncated to $(N_\varphi)^N$ terms,

$$f(\boldsymbol{\varphi}) \approx \tilde{f}_\varphi(\boldsymbol{\varphi}) = \sum_{i_1=-\frac{N_\varphi-1}{2}}^{\frac{N_\varphi-1}{2}} \cdots \sum_{i_N=-\frac{N_\varphi-1}{2}}^{\frac{N_\varphi-1}{2}} f(\varphi_{i_1}, \ldots, \varphi_{i_N}) \times u_K(\varphi_1 - \varphi_{i_1}) \ldots u_K(\varphi_N - \varphi_{i_N}), \tag{B22}$$

where $\varphi_{i_j} = i_j \Delta_\varphi$, $\Delta_\varphi = \frac{\pi}{K}$, and $N_\varphi = \lceil \frac{2}{\pi} KF \rceil$.

Analogously to Eq. (B1), the difference between a N-dimensional function $f(\boldsymbol{\varphi}) \in S(\mathbb{R}^N)$ and its truncated Nyquist-Shannon sampled approximation $\tilde{f}_\varphi(\boldsymbol{\varphi})$ defined by Eq. (B22) is given by

$$f(\boldsymbol{\varphi}) - \tilde{f}_\varphi(\boldsymbol{\varphi}) = w_{\boldsymbol{K}}^f(\boldsymbol{\varphi}) - v(\boldsymbol{\varphi}) + t(\boldsymbol{\varphi}), \tag{B23}$$

where

$$v(\boldsymbol{\varphi}) = \sum_{\boldsymbol{i}=-\infty}^{\infty} w_{\boldsymbol{K}}(\boldsymbol{\varphi_i}) u_{\boldsymbol{K}}(\boldsymbol{\varphi} - \boldsymbol{\varphi_i}), \tag{B24}$$

$$t(\boldsymbol{\varphi}) = \sum_{\boldsymbol{i}=-\infty}^{\infty} w_{\boldsymbol{F}}(\boldsymbol{\varphi_i}) u_{\boldsymbol{K}}(\boldsymbol{\varphi} - \boldsymbol{\varphi_i}). \tag{B25}$$

The following notation was used in Eqs. (B24) and (B25):

$$u_{\boldsymbol{K}}(\boldsymbol{\varphi}) = u_K(\varphi_1) u_K(\varphi_2) \cdots u_K(\varphi_N)$$
$$\boldsymbol{i} = \{i_1, i_2, \ldots, i_N\}.$$

The norm of the tail vector $|w_{\boldsymbol{K}}^f\rangle$ is bounded as

$$\begin{aligned}\left\|w_{\boldsymbol{K}}^f\right\|^2 &\leqslant \sum_{j=1}^{N} \int d\kappa_1 \left(\int_{-\infty}^{-K} d\kappa_j + \int_{K}^{\infty} d\kappa_j\right) \cdots \int d\kappa_N |\hat{f}(\kappa_1, \ldots, \kappa_j, \ldots, \kappa_N)|^2 \\ &= \sum_{j=1}^{N} \left(\int_{-\infty}^{-K} \langle\kappa_j|\rho_j^f|\kappa_j\rangle\, d\kappa_j + \int_{K}^{\infty} \langle\kappa_j|\rho_j^f|\kappa_j\rangle\, d\kappa_j\right) \\ &= \sum_{j=1}^{N} {w_{jK}^f}^2,\end{aligned} \tag{B26}$$

where

$$\rho_j^f = \mathrm{Tr}_{1,2,\ldots,j-1,j+1,\ldots,N}(|f\rangle\langle f|), \tag{B27}$$

is the local density operator at site j obtained by tracing over all other sites and

$${w_{jK}^f}^2 = \int_{-\infty}^{-K} \langle\kappa|\rho_j^f|\kappa\rangle\, d\kappa + \int_{K}^{\infty} \langle\kappa|\rho_j^f|\kappa\rangle\, d\kappa \tag{B28}$$

is the tail weight of $\hat{f}(\boldsymbol{\kappa})$ at site j.

To estimate $\|v\|$, we write $|v\rangle$ in the conjugate-field basis. The Fourier transform of Eq. (B24) yields

$$v(\boldsymbol{\kappa}) = \sum_{\boldsymbol{n}} v_{\boldsymbol{n}}(\boldsymbol{\kappa}), \tag{B29}$$

where

$$v_{\boldsymbol{n}}(\boldsymbol{\kappa}) = R_{\boldsymbol{K}}(\boldsymbol{\kappa})(-1)^{n_1+n_2+\cdots+n_N} w_{\boldsymbol{K}}(\boldsymbol{\kappa} + 2\boldsymbol{n}\boldsymbol{K}), \tag{B30}$$

with $R_{\boldsymbol{K}}(\boldsymbol{\kappa}) = 1$ for $\boldsymbol{\kappa} \in [-\boldsymbol{K}, \boldsymbol{K}]$ and zero otherwise. The norm of $v_{\boldsymbol{n}}$ is

$$||v_{\boldsymbol{n}}||^2 = \int_{-K}^{K} d\kappa_1 \cdots \int_{-K}^{K} d\kappa_N |w_{\boldsymbol{K}}(\boldsymbol{\kappa} + 2\boldsymbol{nK})|^2 = \int_{2\boldsymbol{nK}-\boldsymbol{K}}^{2\boldsymbol{nK}+\boldsymbol{K}} |w_{\boldsymbol{K}}(\boldsymbol{\kappa})|^2 d\boldsymbol{\kappa}. \tag{B31}$$

Now consider the function $\boldsymbol{\kappa}\hat{f}(\boldsymbol{\kappa}) \equiv \kappa_1 \ldots \kappa_n \hat{f}(\kappa_1, \ldots, \kappa_n) \in S(\mathbb{R}^N)$. The tail weight of $\boldsymbol{\kappa}\hat{f}(\boldsymbol{\kappa})$ outside the interval $[-\boldsymbol{K}, \boldsymbol{K}]$, denoted by $r^f_{\boldsymbol{K}}$ is

$$r^{f\,2}_{\boldsymbol{K}} = \sum_{\boldsymbol{n}} \int_{2n_1K-K}^{2n_1K+K} d\kappa_1 \kappa_1^2 \cdots \int_{2n_NK-K}^{2n_NK+K} d\kappa_N \kappa_N^2 |w_{\boldsymbol{K}}(\boldsymbol{\kappa})|^2. \tag{B32}$$

The following inequality is true:

$$r^{f\,2}_{\boldsymbol{K}} \geqslant K^{2N} \sum_{\boldsymbol{n}} c(\boldsymbol{n})^2 \int_{2\boldsymbol{nK}-\boldsymbol{K}}^{2\boldsymbol{nK}+\boldsymbol{K}} |w_{\boldsymbol{K}}(\boldsymbol{\kappa})|^2 d\boldsymbol{\kappa} = K^{2N} \sum_{\boldsymbol{n}} c(\boldsymbol{n})^2 ||v_{\boldsymbol{n}}||^2, \tag{B33}$$

where

$$c(\boldsymbol{n}) = c(n_1)c(n_2)\cdots c(n_N), \tag{B34}$$

with $c(n)$ defined by Eq. (B11). Employing the Cauchy-Schwartz inequality

$$\sum_{\boldsymbol{n}} |v_{\boldsymbol{n}}(\boldsymbol{\kappa})| = \sum_{\boldsymbol{n}} |v_{\boldsymbol{n}}(\boldsymbol{\kappa})||c(\boldsymbol{n})| \frac{1}{|c(\boldsymbol{n})|} \leqslant \sqrt{\sum_{\boldsymbol{n}} |v_{\boldsymbol{n}}(\boldsymbol{\kappa})|^2 |c(\boldsymbol{n})|^2} \sqrt{\sum_{\boldsymbol{n}} \frac{1}{|c(\boldsymbol{n})|^2}} \tag{B35}$$

and

$$\sum_{\boldsymbol{n}\neq\boldsymbol{0}} \frac{1}{|c(\boldsymbol{n})|^2} = \left(2\sum_{n>0} \frac{1}{(2n-1)^2} + 1\right)^N - 1 = \left(\frac{\pi^2}{4} + 1\right)^N - 1, \tag{B36}$$

one gets

$$||v|| \leqslant \left(\frac{\pi^2}{4} + 1\right)^{N/2} \frac{r^f_{\boldsymbol{K}}}{K^N}. \tag{B37}$$

Using Eq. (B25) and the orthogonality properties of *sinc* functions, one gets

$$\|t\|^2 = \int |t(\boldsymbol{\varphi})|^2 d\boldsymbol{\varphi} = \Delta_\varphi^N \sum_{\boldsymbol{i}=-\infty}^{\infty} |w_{\boldsymbol{F}}(\boldsymbol{\varphi_i})|^2, \tag{B38}$$

$$\begin{aligned}
\|t\|^2 &\leqslant \sum_{j=1}^{N} \Delta_\varphi^N \sum_{i_1=\infty}^{\infty} \cdots \sum_{|i_j|>\frac{N_\varphi-1}{2}} \cdots \sum_{i_N=\infty}^{\infty} |f(\varphi_{i_1}, \ldots, \varphi_{i_j}, \ldots, \varphi_{i_N})|^2 \\
&\approx \sum_{j=1}^{N} \int_{-\infty}^{\infty} d\varphi_1 \cdots \sum_{|i_j|>\frac{N_\varphi-1}{2}} \Delta_\varphi \cdots \int_{-\infty}^{\infty} d\varphi_N f(\varphi_1, \ldots, \varphi_{i_j}, \ldots, \varphi_N)|^2 \\
&\approx \sum_{j=1}^{N} \sum_{|i_j|>\frac{N_\varphi-1}{2}} \Delta_\varphi \langle \varphi_{i_j}|\rho_j^f|\varphi_{i_j}\rangle \\
&\approx \sum_{j=1}^{N} \left[w^{f\,2}_{jF} + \frac{\Delta_\varphi}{2}\left(\langle -F|\rho_j^f|-F\rangle + \langle F|\rho_j^f|F\rangle\right)\right],
\end{aligned} \tag{B39}$$

where

$$w^{f\,2}_{jF} = \int_{-\infty}^{-F} d\varphi \langle \varphi|\rho_j^f|\varphi\rangle + \int_{F}^{\infty} d\varphi \langle \varphi|\rho_j^f|\varphi\rangle \tag{B40}$$

is the tail weight of $f(\boldsymbol{\varphi})$ at site j. Analogously to Eq. (B16), in Eq. (B39) we used the Euler-Maclaurin integration rule to approximate the Riemann sum with the integral.

Employing Eqs. (B23), (B26), (B37), and (B39), one has

$$\|f - \tilde{f}_\varphi\| \leqslant \sum_{j=1}^{N} \left[w^f_{jK} + w^f_{jF} + \sqrt{\frac{\pi}{2K}\left(\langle -F|\rho_j^f|-F\rangle + \langle F|\rho_j^f|F\rangle\right)}\right] + \left(\frac{\pi^2}{4} + 1\right)^{N/2} \frac{r^f_{\boldsymbol{K}}}{K^N}. \tag{B41}$$

Similarly, $|f\rangle$ can be approximated by the field-limited function $|\tilde{f}_\kappa\rangle$ defined as

$$\hat{f}(\boldsymbol{\kappa}) \approx \tilde{f}_\kappa(\boldsymbol{\kappa}) = \sum_{p_1=-\frac{N_\varphi-1}{2}}^{\frac{N_\varphi-1}{2}} \cdots \sum_{p_N=-\frac{N_\varphi-1}{2}}^{\frac{N_\varphi-1}{2}} \hat{f}(\kappa_{p_1},\ldots,\kappa_{p_N}) u_F(\kappa_1-\kappa_{p_1})\cdots u_F(\kappa_N-\kappa_{p_N}), \tag{B42}$$

where $\kappa_{p_j} = p_j\Delta_\kappa$, $\Delta_\kappa = \frac{\pi}{F}$. The error of the approximation is bounded as

$$\|f-\tilde{f}_\kappa\| \leqslant \sum_{j=1}^{N}\left[w_{jF}^f + w_{jK}^f + \sqrt{\frac{\pi}{2F}\left(\langle -K|\rho_j^f|-K\rangle + \langle K|\rho_j^f|K\rangle\right)}\right] + \left(\frac{\pi^2}{4}+1\right)^{N/2}\frac{r_{\boldsymbol{F}}^f}{F^N}, \tag{B43}$$

where $r_{\boldsymbol{F}}^f$ is the weight of $\varphi_1\varphi_2\cdots\varphi_N f(\varphi_1,\ldots,\varphi_N)$ outside the N-dimensional sampling interval $[-\boldsymbol{F},\boldsymbol{F}]$,

$$r_{\boldsymbol{F}}^{f\,2} = \int d\varphi_1\cdots\int d\varphi_N\varphi_1^2\cdots\varphi_N^2|w_{\boldsymbol{F}}(\varphi_1,\ldots,\varphi_N)|^2. \tag{B44}$$

APPENDIX C: ALIASING AND FINITE FOURIER TRANSFORM

1. Aliased functions

Consider a function $f(\varphi)\in L^2(\mathbb{R})$ and its Fourier transform $\hat{f}(\kappa)$ given by Eq. (5). Consider also a set of N_φ field sampling points $\{\varphi_i = i\Delta_\varphi\}_i$ with $i = \overline{-\frac{N_\varphi-1}{2},\frac{N_\varphi-1}{2}}$ and a set of N_φ conjugate-field sampling points $\{\kappa_p = p\Delta_\kappa\}_p$ with $p = \overline{-\frac{N_\varphi-1}{2},\frac{N_\varphi-1}{2}}$, where the discretization intervals are chosen such that $\Delta_\varphi\Delta_\kappa = \frac{2\pi}{N_\varphi}$.

Here we will show that the aliased functions at the sampling points,

$$f_a(\varphi_i) = \sqrt{\Delta_\varphi}\sum_{n=-\infty}^{\infty}(-1)^n f(\varphi_i + nN_\varphi\Delta_\varphi), \tag{C1}$$

$$\hat{f}_a(\kappa_p) = \sqrt{\Delta_\kappa}\sum_{n=-\infty}^{\infty}(-1)^n \hat{f}(\kappa_p + nN_\varphi\Delta_\kappa) \tag{C2}$$

are related via a finite Fourier transform,

$$\hat{f}_a(\kappa_p) = (\tilde{\mathcal{F}}f_a)(\kappa_p) \equiv \frac{1}{\sqrt{N_\varphi}}\sum_{j=-\frac{N_\varphi-1}{2}}^{\frac{N_\varphi-1}{2}} f_a(\varphi_j)e^{-i\kappa_p\varphi_j} \tag{C3}$$

and

$$f_a(\varphi_j) = (\tilde{\mathcal{F}}^{-1}\hat{f}_a)(\varphi_j) \equiv \frac{1}{\sqrt{N_\varphi}}\sum_{p=-\frac{N_\varphi-1}{2}}^{\frac{N_\varphi-1}{2}} \hat{f}_a(\kappa_p)e^{i\kappa_p\varphi_j}. \tag{C4}$$

The proof of Eq. (C3) and Eq. (C4) is similar to the one presented in Ref. [44] and is sketched below.

The value of the function $f(\varphi)$ at $\{\varphi_i = (i+1/2)\Delta_\varphi\}_{i=\overline{-\infty,\infty}}$ is given by

$$\begin{aligned} f(\varphi_i) &= \frac{1}{\sqrt{2\pi}}\sum_{n=-\infty}^{\infty}\int_{-K+2nK}^{K+2nK}\hat{f}(\kappa)e^{i\kappa\varphi_i}d\kappa \\ &= \frac{1}{\sqrt{2\pi}}\sum_{n=-\infty}^{\infty}\int_{-K}^{K}(-1)^n\hat{f}(\kappa+nN_\varphi\Delta_\kappa)e^{i\kappa\varphi_i}d\kappa, \end{aligned} \tag{C5}$$

where $K = N_\varphi\Delta_\kappa/2$. Equation (C5) reads

$$f(\varphi_i) = \frac{1}{\sqrt{2\pi\,\Delta_\kappa}}\int_{-K}^{K}\hat{f}_a(\kappa)e^{i\kappa\varphi_i}, \tag{C6}$$

where

$$\hat{f}_a(\kappa) \equiv \sqrt{\Delta_\kappa}\sum_{n=-\infty}^{\infty}(-1)^n\hat{f}(\kappa+nN_\varphi\Delta_\kappa). \tag{C7}$$

Since $\hat{f}_a(\kappa)$ defined by Eq. (C7) is antiperiodic, i.e., $\hat{f}_a(\kappa) = -\hat{f}_a(\kappa+N_\varphi\Delta_\kappa)$, it can be written as

$$\hat{f}_a(\kappa) = \sqrt{\Delta_\kappa}\frac{\Delta_\varphi}{\sqrt{2\pi}}\sum_{i=-\infty}^{\infty}f(\varphi_i)e^{-i\kappa\varphi_i}. \tag{C8}$$

The value of $\hat{f}_a(\kappa)$ at the sampling points $\{\kappa_p\}_{p=\overline{-\frac{N_\varphi-1}{2},\frac{N_\varphi-1}{2}}}$ is given by

$$\begin{aligned} \hat{f}_a(\kappa_p) = \sqrt{\Delta_\varphi}\sqrt{\frac{\Delta_\varphi\Delta_\kappa}{2\pi}}\sum_{n=-\infty}^{\infty}\sum_{i=-\frac{N_\varphi-1}{2}}^{\frac{N_\varphi-1}{2}} \\ \times\ (-1)^n f(\varphi_i+nN_\varphi\Delta_\varphi)e^{-i\kappa_p\varphi_i}, \end{aligned} \tag{C9}$$

which implies Eq. (C3). Analogously, Eq. (C4) can be derived.

2. Finite Fourier transform approximation for the continuous Fourier transform

The difference between the vector defined by the sampling points of a function and the vector defined by the aliased function is given by the function's values outside the sampling

interval. For example,

$$\Delta_\varphi \sum_{i=-\frac{N_\varphi-1}{2}}^{\frac{N_\varphi-1}{2}} |f_a(\varphi_i) - f(\varphi_i)|^2 = \Delta_\varphi \sum_{n=-\infty}^{\infty} \sum_{i=-\frac{N_\varphi-1}{2}}^{\frac{N_\varphi-1}{2}} \left|w_F^f(\varphi_i + nN_\varphi\Delta_\varphi)\right|^2 = \Delta_\varphi \sum_{i=-\infty}^{\infty} \left|w_F^f(\varphi_i)\right|^2$$

$$\approx \left\|w_F^f\right\|^2 + \frac{\Delta_\varphi}{2}\left[|f(-F)|^2 + |f(F)|^2\right], \tag{C10}$$

where the same approximation as in Eq. (B16) was made. Similarly,

$$\Delta_\kappa \sum_{p=-\frac{N_\varphi-1}{2}}^{\frac{N_\varphi-1}{2}} |\hat{f}_a(\kappa_p) - \hat{f}(\kappa_p)|^2 = \Delta_\kappa \sum_{n=-\infty}^{\infty} \sum_{p=-\frac{N_\varphi-1}{2}}^{\frac{N_\varphi-1}{2}} \left|w_K^f(\kappa_p + nN_\varphi\Delta_\kappa)\right|^2 = \Delta_\kappa \sum_{p=-\infty}^{\infty} \left|w_K^f(\kappa_p)\right|^2$$

$$\approx \left\|w_K^f\right\|^2 + \frac{\Delta_\kappa}{2}\left[|\hat{f}(-K)|^2 + |\hat{f}(K)|^2\right]. \tag{C11}$$

The difference between the finite Fourier transform of the set $\{f(\varphi_i)\}_i$ and the vector defined by the function $\hat{f}(\kappa)$ at the conjugate-field sampling points is given by

$$\Delta_\kappa \sum_{p=-\frac{N_\varphi-1}{2}}^{\frac{N_\varphi-1}{2}} |\tilde{\mathcal{F}}f(\kappa_p) - \hat{f}(\kappa_p)|^2 = \Delta_\kappa \sum_{p=-\frac{N_\varphi-1}{2}}^{\frac{N_\varphi-1}{2}} |(\tilde{\mathcal{F}}f)(\kappa_p) - (\tilde{\mathcal{F}}f_a)(\kappa_p) + \hat{f}_a(\kappa_p) - \hat{f}(\kappa_p)|^2$$

$$\leqslant 2\Delta_\kappa \sum_{p=-\frac{N_\varphi-1}{2}}^{\frac{N_\varphi-1}{2}} |(\tilde{\mathcal{F}}f)(\kappa_p) - (\tilde{\mathcal{F}}f_a)(\kappa_p)|^2 + 2\Delta_\kappa \sum_{p=-\frac{N_\varphi-1}{2}}^{\frac{N_\varphi-1}{2}} |\hat{f}_a(\kappa_p) - \hat{f}(\kappa_p)|^2$$

$$= 2\Delta_\varphi \sum_{i=-\frac{N_\varphi-1}{2}}^{\frac{N_\varphi-1}{2}} |f(\varphi_i) - f_a(\varphi_i)|^2 + 2\Delta_\kappa \sum_{p=-\frac{N_\varphi-1}{2}}^{\frac{N_\varphi-1}{2}} |\hat{f}_a(\kappa_p) - \hat{f}(\kappa_p)|^2$$

$$\approx 2\left(\left\|w_F^f\right\|^2 + \left\|w_K^f\right\|^2\right)$$

$$+ \frac{\pi}{K}\left[|f(-F)|^2 + |f(F)|^2\right] + \frac{\pi}{F}\left[|\hat{f}(-K)|^2 + |\hat{f}(K)|^2\right]. \tag{C12}$$

In the first line of Eq. (C12), we added and subtracted the aliased function $\hat{f}_a(\kappa_p) = (\tilde{\mathcal{F}}f_a)(\kappa_p)$. In the last line of Eq. (C12), we used Eq. (C10) and Eq. (C11).

APPENDIX D: BAND-LIMITED WAVE FUNCTION WITH LARGE NUMBER OF BOSONS

For our example in Sec. III C, we construct a band-limited function

$$f(\varphi) = \sum_i a_i u_K(\varphi - \varphi_i) \tag{D1}$$

where we take $F = K = \sqrt{\pi N_\varphi/2}$ [see Eq. (15)], with $N_\varphi = 64$.

When the summation over i is restricted to a finite set, $|f(\varphi)|$ decays as least as $|\varphi|^{-1}$ with increasing $|\varphi|$ [since $u_K(\varphi) \propto \varphi^{-1}$; see Eq. (A7)]. As described below, we choose the coefficients a_i such that $|f(\varphi)|$ decays as $|\varphi|^{-8}$ at large $|\varphi|$. Let's first take all the coefficients $a_i = 0$ except for the one corresponding to the indices $i = \pm q_1$, (where q_1 is an arbitrary half-integer). If $a_{\pm q_1} = 1$, one gets

$$f_{q_1}(\varphi) = \frac{1}{\sqrt{2\Delta_\varphi}}\left[\frac{\sin\left(\frac{\pi\varphi}{\Delta_\varphi} - q_1\pi\right)}{\frac{\pi\varphi}{\Delta_\varphi} - q_1\pi} + \frac{\sin\left(\frac{\pi\varphi}{\Delta_\varphi} + q_1\pi\right)}{\frac{\pi\varphi}{\Delta_\varphi} + q_1\pi}\right]$$

$$= -2\frac{1}{\sqrt{2\Delta_\varphi}}\sin\left(\frac{\pi\varphi}{\Delta_\varphi} - \frac{\pi}{2}\right)\left[q_1\frac{\Delta_\varphi^2}{\pi\varphi^2} + 6q_1^3\frac{\Delta_\varphi^4}{\pi\varphi^4}\right.$$

$$\left. + 120q_1^5\frac{\Delta_\varphi^6}{\pi\varphi^6} + 5040q_1^7\frac{\Delta_\varphi^8}{\pi\varphi^8} + O\left(\frac{\Delta_\varphi^{10}}{\varphi^{10}}\right)\right]. \tag{D2}$$

The function $f_{q_1}(\varphi)$ decays as $|\varphi|^{-2}$ with increasing $|\varphi|$. We define our function as

$$f(\varphi) = c_1 f_{q_1}(\varphi) + c_2 f_{q_2}(\varphi) + c_3 f_{q_3}(\varphi) + c_4 f_{q_4}(\varphi)$$

$$+ c_5 f_{q_5}(\varphi) + c_6 f_{q_6}(\varphi)$$

$$+ c_7 f_{q_7}(\varphi) + c_8 f_{q_8}(\varphi), \tag{D3}$$

where $q_1, \ldots, q_8$ are half-integer smaller than $N_\varphi/3$ and $c_1, \ldots, c_8$ are chosen such that the terms proportional to $|\varphi|^{-2}$,

$|\varphi|^{-4}$, and $|\varphi|^{-6}$ cancel out. The function can be written as

$$f(\varphi) = c_f \sin\left(\frac{\pi\varphi}{\Delta_\varphi} - \frac{\pi}{2}\right)\frac{\Delta_\varphi^8}{\pi\varphi^8} + O\left(\frac{\Delta_\varphi^{10}}{\pi\varphi^{10}}\right). \tag{D4}$$

where c_f is a normalization constant term depending on $q_1, \ldots, q_8$ and Δ_φ.

APPENDIX E: INEQUALITIES FOR LOCAL BOSON DISTRIBUTION MEASUREMENT

The probability to measure a certain integer k on the ancillary register depends on the quantity a_{nk} defined by Eq. (120).

We have

$$|a_{nk}| = \left|\frac{1}{2^{n_r}}\sum_{x=0}^{2^{n_r}-1} e^{-i\frac{2\pi}{2^{n_r}}\mu_{nk}x}\right| = \frac{1}{2^{n_r}}\frac{|\sin(\pi\mu_{nk})|}{|\sin\left(\frac{\pi\mu_{nk}}{2^{n_r}}\right)|} \tag{E1}$$

with

$$\mu_{nk} = \frac{\tilde{E}_n}{m_0} - k. \tag{E2}$$

The following properties of a_{nk} are true:

(1) $|a_{nk}| = 1$ when $\mu_{nk} = 0$. It can be checked by direct substitution in the first part of Eq. (E1).

(2) $|a_{nk}| \leqslant 1$. It follows from the inequality $|\sin(Mx)| \leqslant M|\sin(x)|$, which holds for any integer $M > 1$ and any x (it can be easily proven by induction). In Eq. (E1) one needs to take $M = 2^{n_r}$ and $x = \pi\mu_{nk}/2^{n_r}$.

(3) $|a_{nk}| \geqslant 2/\pi$ when $|\mu_{nk}| \leqslant 1/2$. The proof is similar to the one in Refs [13,14] for estimating the probability to measure the nearest integer to the phase factor in a QPE algorithm. The inequality $|x| \geqslant |\sin(x)|$ implies

$$|a_{nk}| \geqslant \frac{1}{2^{n_r}}\frac{|\sin(\pi\mu_{nk})|}{|\frac{\pi\mu_{nk}}{2^{n_r}}|} = \frac{|\sin(\pi\mu_{nk})|}{|\pi\mu_{nk}|}. \tag{E3}$$

Furthermore, the inequality $|\sin(x)| \geqslant |2x/\pi|$, which holds for $|x| \leqslant \pi/2$ [on the interval $[0, \pi/2]$ $\sin(x)$, is above the line connecting $(0, 0)$ and $(\pi/2, 1)$] implies

$$|a_{nk}| \geqslant \frac{2}{\pi} \quad \text{for} \quad |\mu_{nk}| \leqslant \frac{1}{2}. \tag{E4}$$

For any $n \geqslant N_b$ we have $\mu_{nk} \leqslant 1/2$ when k is the nearest integer to $\tilde{E}_n/m_0$. Thus for any $n \geqslant N_b$ there is always a k such that Eq. (E4) is true. That implies

$$\max_{k \geqslant N_b} |a_{nk}|^2 \geqslant \frac{4}{\pi^2}. \tag{E5}$$

[1] V. Privman, *Finite Size Scaling and Numerical Simulation of Statistical Systems* (World Scientific, Singapore, 1990).

[2] J. L. Cardy, *Finite Size Scaling* (Elsevier, Amsterdam, 2012), Vol. 2.

[3] S. P. Jordan, K. S. M. Lee, and J. Preskill, Science **336**, 1130 (2012).

[4] S. P. Jordan, K. S. M. Lee, and J. Preskill, Quantum Inf. Comput. **14**, 1014 (2014).

[5] R. D. Somma, Quantum Inf. Comput. **16**, 1125 (2016).

[6] A. Macridin, P. Spentzouris, J. Amundson, and R. Harnik, Phys. Rev. Lett. **121**, 110504 (2018).

[7] A. Macridin, P. Spentzouris, J. Amundson, and R. Harnik, Phys. Rev. A **98**, 042312 (2018).

[8] N. Klco and M. J. Savage, Phys. Rev. A **99**, 052335 (2019).

[9] P. Jaming, A. Karoui, and S. Spektor, J. Approx. Theory **212**, 41 (2016).

[10] D. Slepian, Proc. IEEE **64**, 292 (1976).

[11] H. J. Landau and H. O. Pollak, Bell Syst. Tech. J. **41**, 1295 (1962).

[12] J. B. Altepeter, D. F. James, and P. G. Kwiat, in *Quantum State Estimation*, edited by M. Paris and J. Řeháček (Springer, Berlin, 2004), pp. 113–145.

[13] M. A. Nielsen and I. L. Chuang, *Quantum Computation and Quantum Information: 10th Anniversary Edition* (Cambridge University Press, Cambridge, 2010).

[14] R. Cleve, A. Ekert, C. Macchiavello, and M. Mosca, Proc. R. Soc. London A **454**, 339 (1998).

[15] N. P. D. Sawaya, T. Menke, T. H. Kyaw, S. Johri, A. Aspuru-Guzik, and G. G. Guerreschi, npj Quantum Inf. **6**, 49 (2020).

[16] A. Barenco, C. H. Bennett, R. Cleve, D. P. DiVincenzo, N. Margolus, P. Shor, T. Sleator, J. A. Smolin, and H. Weinfurter, Phys. Rev. A **52**, 3457 (1995).

[17] V. V. Shende, I. L. Markov, and S. S. Bullock, Phys. Rev. A **69**, 062321 (2004).

[18] A. M. Krol, A. Sarkar, I. Ashraf, Z. Al-Ars, and K. Bertels, arXiv:2101.02993.

[19] A. Li, A. Macridin, P. Spentzouris, and S. Mrenna (unpublished).

[20] F. Gieres, Rep. Prog. Phys. **63**, 1893 (2000).

[21] J. Becnel and A. Sengupta, Mathematics **3**, 527 (2015).

[22] R. B. Melrose, Differential analysis lecture notes (2017), https://klein.mit.edu/~rbm/18.155-F16/.

[23] W. D. Van Suijlekom, *Schwartz Space*, From MathWorld–A Wolfram Web Resource, created by Eric W. Weisstein, https://mathworld.wolfram.com/SchwartzSpace.html.

[24] C. E. Shannon, Proc. IRE **37**, 10 (1949).

[25] S. Engelberg, in *Digital Signal Processing: An Experimental Approach*, Signals and Communication Technology (Springer, London, 2008), pp. 21–27.

[26] I. Gradshteyn and I. Ryzhik, in *Table of Integrals, Series, and Products*, edited by I. Gradshteyn and I. Ryzhik (Academic Press, Singapore, 1980).

[27] A. Osipov, V. Rokhlin, and H. Xiao, *Prolate Spheroidal Wave Functions of Order Zero: Mathematical Tools for Bandlimited Approximation*, Applied Mathematical Sciences (Springer US, New York, 2013), Vol. 187.

[28] C. Gerry and P. Knight, *Introductory Quantum Optics* (Cambridge University Press, Cambridge, 2004).

[29] J. R. McClean, J. Romero, R. Babbush, and A. Aspuru-Guzik, New J. Phys. **18**, 023023 (2016).

[30] M. Cramer, M. B. Plenio, S. T. Flammia, R. Somma, D. Gross, S. D. Bartlett, O. Landon-Cardinal, D. Poulin, and Y.-K. Liu, Nat. Commun. **1**, 149 (2010).

[31] B. P. Lanyon, C. Maier, M. Holzäpfel, T. Baumgratz, C. Hempel, P. Jurcevic, I. Dhand, A. S. Buyskikh, A. J. Daley, M. Cramer *et al.*, Nat. Phys. **13**, 1158 (2017).

[32] J. G. Titchener, M. Gräfe, R. Heilmann, A. S. Solntsev, A. Szameit, and A. A. Sukhorukov, npj Quantum Inf. **4**, 19 (2018).

[33] H. Häffner, W. Hänsel, C. F. Roos, J. Benhelm, D. Chek-al-kar, M. Chwalla, T. Körber, U. D. Rapol, M. Riebe, P. O. Schmidt *et al.*, Nature (London) **438**, 643 (2005).

[34] C. Song, K. Xu, W. Liu, C.-p. Yang, S.-B. Zheng, H. Deng, Q. Xie, K. Huang, Q. Guo, L. Zhang *et al.*, Phys. Rev. Lett. **119**, 180511 (2017).

[35] T. Häner, M. Roetteler, and K. M. Svore, arXiv:1805.12445.

[36] M. K. Bhaskar, S. Hadfield, A. Papageorgiou, and I. Petras, Quantum Inf. Comput. **16**, 0197 (2016).

[37] F. Arute *et al.* (Google AI Quantum Collaborators), arXiv:2010.07965 (2020).

[38] P. Jurcevic, A. Javadi-Abhari, L. S. Bishop, I. Lauer, D. F. Bogorin, M. Brink, L. Capelluto, O. Günlük, T. Itoko, N. Kanazawa *et al.*, Quantum Sci. Technol. **6**, 025020 (2021).

[39] Y. Kim, C. J. Wood, T. J. Yoder, S. T. Merkel, J. M. Gambetta, K. Temme, and A. Kandala, arXiv:2108.09197.

[40] F. Arute, K. Arya, R. Babbush, D. Bacon, J. C. Bardin, R. Barends, A. Bengtsson, S. Boixo, M. Broughton, B. B. Buckley *et al.*, arXiv:2010.07965.

[41] C. Cîrstoiu, Z. Holmes, J. Iosue, L. Cincio, P. J. Coles, and A. Sornborger, npj Quantum Inf. **6**, 82 (2020).

[42] M. Benedetti, M. Fiorentini, and M. Lubasch, Phys. Rev. Research **3**, 033083 (2021).

[43] P. DeVries and J. Hasbun, *A First Course in Computational Physics* (Jones & Bartlett Learning, Sudbury Massachusetts, 2011).

[44] J. Cooley, P. Lewis, and P. Welch, IEEE Trans. Audio Electroacoust. **15**, 79 (1967).